

The Properties and Evolution of a K-band Selected Sample of Massive Galaxies at $z \sim 0.4 - 2$ in the Palomar/DEEP2 Survey

C. J. Conselice^{1,2*}, K. Bundy^{3,2}, I. Trujillo¹, A. Coil^{4,5}, P. Eisenhardt⁶, R.S. Ellis⁷,
 A. Georgakakis⁸, J. Huang⁹, J. Lotz¹⁰, K. Nandra⁸, J. Newman¹¹,
 C. Papovich^{4,12}, B. Weiner^{13,4}, C. Willmer⁴

¹ *University of Nottingham, School of Physics & Astronomy, Nottingham, NG7 2RD UK*

² *Previous address: Palomar Observatory, Caltech, MC 105-24*

³ *Department of Astronomy, University of Toronto, Canada*

⁴ *Steward Observatory, University of Arizona, Tuscon, AZ*

⁵ *Hubble Fellow*

⁶ *Jet Proportion Laboratory, Caltech, Pasadena, CA*

⁷ *California Institute of Technology, MC 105-24, Pasadena, CA 91125*

⁸ *Imperial College, London*

⁹ *Harvard-Smithsonian Center for Astrophysics, Cambridge, MA*

¹⁰ *NOAO, Tuscon, AZ*

¹¹ *Lawrence Berkeley National Laboratory, Berkeley CA*

¹² *Spitzer Fellow*

¹³ *University of Maryland, College Park MD*

Accepted ; Received ; in original form

ABSTRACT

We present the results of a study on the properties and evolution of massive ($M_* > 10^{11} M_\odot$) galaxies at $z \sim 0.4 - 2$ utilising Keck spectroscopy, Near-Infrared Palomar imaging, and Hubble, Chandra, and Spitzer data covering fields targeted by the DEEP2 galaxy spectroscopic survey. Our sample is K-band selected and stellar mass limited, based on wide-area near-infrared imaging from the Palomar Observatory Wide-Field Infrared Survey, which covers 1.53 deg^2 to a 5σ depth of $K_{s,\text{vega}} \sim 20.5$. Our primary goal is obtaining a broad census of massive galaxies through measuring how their number and mass densities, morphology, as well as their star formation and AGN content evolve from $z \sim 0.4 - 2$. Our major findings include: (i) statistically the mass and number densities of $M_* > 10^{11} M_\odot$ galaxies show little evolution between $z = 0 - 1$, and from $z \sim 0 - 2$ for $M_* > 10^{11.5} M_\odot$ galaxies. We however find significant evolution between $1 < z < 1.5$ for $10^{11} M_\odot < M_* < 10^{11.5} M_\odot$ galaxies. (ii) After examining the structures of our galaxies using Hubble ACS imaging, we find that $M_* > 10^{11} M_\odot$ selected galaxies show a nearly constant elliptical fraction of $\sim 70 - 90\%$ at all redshifts. The remaining objects tend to be peculiars possibly undergoing mergers at $z > 0.8$, while spirals dominate the remainder at lower redshifts. A significant fraction ($\sim 25\%$) of these early-types contain minor structural anomalies. (iii) We find that only a fraction ($\sim 60\%$) of massive galaxies with $M_* > 10^{11} M_\odot$ are on the red-sequence at $z \sim 1.4$, while nearly 100% evolve onto it by $z \sim 0.4$. (iv) By utilising Spitzer MIPS imaging and [OII] line fluxes we argue that $M_* > 10^{11.5} M_\odot$ galaxies have a steeply declining star formation rate density $\sim (1+z)^6$. By examining the contribution of star formation to the evolution of the mass function, as well as the merger history through the CAS parameters, we determine that $M_* > 10^{11} M_\odot$ galaxies undergo on average $0.9_{-0.5}^{+0.7}$ major mergers at $0.4 < z < 1.4$. (v) We find that a high (5%) fraction of all $M_* > 10^{11} M_\odot$ galaxies are X-ray emitters. Roughly half of these are morphologically distorted ellipticals or peculiars. Finally, we compare our mass growth with semi-analytical models from the Millennium simulation, finding relative good agreement at $z < 2$ for the $M_* < 10^{11.5} M_\odot$ systems, but that the number and mass densities of $M_* > 10^{11.5} M_\odot$ galaxies are under predicted by a factor of > 100 .

Key words: Galaxies: Evolution. Formation. Structure. Morphology. Classification

1 INTRODUCTION

Understanding when and how the most massive galaxies in the universe formed is one of the most outstanding problems in cosmology and galaxy formation. Massive galaxies are predicted in Cold Dark Matter based models of structure formation to form gradually with time through the merging of smaller systems (e.g., White & Rees 1978). While there is some evidence for this process (e.g., Le Fevre et al. 2000; Patton et al. 2002; Conselice et al. 2003a,b; Bridge et al. 2007), many details are still lacking. Alternatively, massive galaxies, which are mostly ellipticals in today’s universe (e.g., Conselice 2006a), may have formed in a very rapid collapse of gas (e.g., Larson 1974). Observational evidence suggests that passively evolving massive galaxies exist at $z \sim 1$, as well as at even early times, $z > 2$ (e.g., Dunlop et al. 1996; Spinrad et al. 1997; Fontana et al. 2004; Daddi et al. 2004; Glazebrook et al. 2004; Treu et al. 2005; Labbe et al. 2005; Papovich et al. 2006; Grazian et al. 2006; Kriek et al. 2006; Lane et al. 2007). These systems are a subset of the massive galaxy population at high redshift, yet their nature, and whether or not they can account for all of the most massive galaxies in today’s universe is still unknown. We also do not yet know if these massive galaxies are still forming when the universe was half its current age (at $z \sim 1$).

Massive galaxies are largely the test-bed for galaxy models, and therefore understanding their evolution observationally is an important test of the physics behind galaxy formation. A major part of this problem is determining when massive galaxies form. Some studies claim that massive galaxies are all in place by $z \sim 1$ (e.g., Glazebrook et al. 2004). However, since star formation and merging activity has been seen in ellipticals from $z \sim 0$ to $z \sim 1$ (Stanford et al. 2004; Lin et al. 2004; Teplitz et al. 2006), a definite answer remains elusive. If it were possible to date every star in nearby massive galaxies, we could in principle determine the formation epoch and time-scales of these systems by examining their individual stars. We cannot however resolve all the stars in galaxies, and their integrated stellar properties, such as colours, become degenerate after about 5 Gyrs (e.g., Worthey 1994). Stellar ages in massive galaxies also do not necessarily correlate with the assembly of mass through, for example, merging activity (Conselice 2006b; De Lucia et al. 2006; Trujillo et al. 2006). An alternative approach towards understanding massive galaxies and their evolution is empirically measuring the number densities, morphologies, star formation rates, and stellar masses of the most massive systems at some fiducial time and to compare these to similar quantities at different times (redshifts), and with models.

This has however traditionally been a challenging problem since the most massive galaxies are typically very red, either due to evolved stellar populations, or by formation in dusty starbursts (e.g., Graham & Dey 1996). Because of the shape of the spectral energy distributions of evolved galaxies, they are identifiable at $z \sim 1$ due to their extremely red near-infrared to optical colours. These objects are sometimes known as extremely red objects (Elston et al. 1988), which sample a fraction of $z > 1$ massive galaxies (e.g., Moustakas et al. 2004; Conselice et al. 2007a). Conversely if one can obtain complete redshift samples, and combine these with deep near-infrared imaging, it is possible to locate the most massive galaxies up to $z \sim 1.4$ without relying on assumptions

concerning their spectral energy distributions, morphologies, or star formation histories.

Tracing the total evolution of stellar mass through cosmic time has been attempted in several fields, including the Hubble Deep Fields (Dickinson et al. 2003), the GEMS/COMBO-17 field (Borch et al. 2006), and the GOODS fields (Bundy et al. 2005). Recently there have also been claims for the determination of the stellar mass evolution of galaxies at $z \sim 0 - 3$ (Dickinson et al. 2003; Fontana et al. 2004; Bundy et al. 2006; Rudnick et al. 2006). Some of these studies claim that many massive galaxies are formed by $z \sim 2 - 3$, and that these systems prove to be a complication for Cold Dark Matter models of structure formation (e.g., Glazebrook et al. 2003). There are however several limitations to these studies. The two most important being the use of photometric redshifts, and the small field sizes used in these earlier studies. What is now needed is a large spectroscopic survey over a large area, with deep near-infrared imaging to measure accurate stellar masses of galaxies found when the universe was younger than half its current age. We provide such a study in this paper by utilising ~ 1.5 deg² Palomar NIR imaging of the DEEP2 fields (Davis et al. 2003). We also go beyond previous work by utilising ancillary data on a purely mass selected sample to determine the morphologies, colours, and star formation rates of massive galaxies, and how these properties evolved down to $z \sim 0.4$.

Our galaxies are selected from the Palomar Observatory Wide-Field Infrared survey, which is designed to determine robustly the stellar mass evolution of galaxies, and identify the most massive galaxies, at $0.4 < z < 2$. Previously, we have utilised spectroscopic redshifts from the DEEP2 redshift survey (Davis et al. 2003; Faber et al. 2005) to probe the mass function down to $M^* + 3$ (Bundy et al. 2005, 2006), and to study the properties of distant red galaxies (Conselice et al. 2007). Our goal in this paper is specifically to understand the evolutionary history and properties of high redshift massive galaxies, defined as systems with $M_* > 10^{11} M_\odot$ at $z < 2$. One of our primary objectives is to study systems at $z < 1.4$, where we have ancillary information from other telescopes.

This paper is organised as follows. §2 is a presentation of our data. §3 gives an overview of the methodology used to determine the quantities used in this paper, while §4 is a discussion of the properties and evolution of massive galaxies at $0.4 < z < 1.4$. §5 is a discussion of our results in terms of galaxy evolution scenarios, and §6 is a summary. Throughout this paper we use a standard cosmology of $H_0 = 70$ km s⁻¹ Mpc⁻¹, and $\Omega_m = 1 - \Omega_\lambda = 0.3$. All quoted magnitudes are in the Vega systems, unless otherwise specified.

2 DATA

The galaxies we study in this paper consists of those in the fields covered by the Palomar Observatory Wide-Field Infrared Survey (POWIR, Table 1), excluding the GOODS North field discussed in Bundy et al. (2005). The POWIR survey was designed to obtain deep K-band and J-band data over a significant (~ 1.5 deg²) area. Observations were carried out between September 2002 and October 2005 over a total of ~ 70 nights. This survey covers the GOODS field North (Giavalisco et al. 2004; Bundy et al. 2005), the Ex-

Table 1. The Palomar Fields and WIRC pointings Areas

Field	RA	Dec.	area (arcmin ²)
EGS	14 17 00	+52 30 00	2165
Field 2	16 52 00	+34 55 00	787
Field 3	23 30 00	+00 00 00	984
Field 4	02 30 00	+00 00 00	984

tended Groth Strip (Davis et al. 2006), and three other fields that the DEEP2 team has observed with the DEIMOS spectrograph (Davis et al. 2003). The total area we cover in the K-band is $5524 \text{ arcmin}^2 = 1.53 \text{ deg}^2$, with half of this area imaged in the J-band. Our goal depth was $K_{s,\text{vega}} = 21$, although not all fields are covered this deep, but all have 5σ depths between $K_{s,\text{vega}} = 20.2 - 21.5$ for point sources, measured in a $2''$ diameter aperture. Table 1 lists the DEEP2 fields, and the area we have imaged in each. For our purposes we will abbreviate the fields covered as: EGS (Extended Groth Strip), Field 2, Field 3, and Field 4.

All of our K_s -band data were acquired utilising the WIRC camera on the Palomar 5 meter telescope. WIRC has an effective field of view of $8.1' \times 8.1'$, with a pixel scale of $0.25'' \text{ pixel}^{-1}$. Our total survey contains 75 WIRC pointings. During the K_s -band observations we used 30 second integrations, with four exposures per pointing. The J-band observations were taken with 120 second exposures per pointing. Typical total exposure times were between one and two hours for both bands. Our reduction procedure follows standard method for combining NIR ground-based imaging, and is described in more detail in Bundy et al. (2006). The resulting seeing FWHM in the K_s -band imaging ranges from $0.8''$ to $1.2''$, and is typically $1.0''$.

Photometric calibration was carried out by referencing Persson et al. (1998) standard stars during photometric conditions. The final images were made by combining individual mosaics obtained over several nights. The K_s -band mosaics are comprised of coadditions of 4×30 second exposures dithered over a non-repeating $7.0''$ pattern. The images were processed using a double-pass reduction pipeline we developed specifically for WIRC. For galaxy detection and photometry we utilised the SExtractor package (Bertin & Arnouts 1996). False artifacts are removed through SExtractor flags which identify sources that do not have normal galaxy or stellar profiles. From this we construct a K-selected sample, which is then cross-referenced with the DEEP2 redshift catalog.

Other data used in this paper consists of: optical imaging from the CFHT over all fields, MIPS imaging from the *Spitzer Space Telescope*, imaging from the Advanced Camera for Surveys (ACS) on Hubble, Chandra X-ray imaging, and spectroscopy from the DEIMOS spectrograph on the Keck II telescope (Davis et al. 2003). A summary of these ancillary data sets, which are mostly within the Extended Groth Strip, are presented in Davis et al. (2006).

The optical imaging of our fields comes from the CFHT 3.6-m, and consists of data in the B, R and I bands taken with the CFH12K camera - a $12,288 \times 8,192$ pixel CCD mosaic with a pixel scale of $0.21''$. The integration times for these observations are 1 hour in B and R, and 2 hours in I, per pointing, with a R-band 5σ depth of $R_{AB} \sim 25.1$, and

similar depths at B and I (Coil et al. 2004b). The details of the data reduction for this data is described in Coil et al. (2004b). From this imaging data a $R_{AB} = 24.1$ magnitude limit was used for determining targets for the DEEP2 spectroscopy. The details for how these imaging data were acquired and reduced are covered in Coil et al. (2004b). The seeing for the optical imaging is roughly the same as that for the NIR imaging, and we measure photometry consistently using a $2''$ diameter aperture.

The Keck spectra were acquired with the DEIMOS spectrograph (Faber et al. 2003) as part of the DEEP2 redshift survey (Davis et al. 2003). The selection for targets for the DEEP2 spectroscopy was based on the optical properties of the galaxies detected in the CFHT photometry, with the basic selection criteria $R_{AB} < 24.1$. Spectroscopy in the EGS was acquired through this magnitude limit, with no strong colour cuts applied to the selection. Objects in Fields 2-4 were selected for spectroscopy based on their position in $(B - R)$ vs. $(R - I)$ colour space to focus on galaxies at redshifts $z > 0.7$. The total survey includes over 30,000 galaxies with a secure redshift, with about a third of these in the EGS field. In all fields the sampling rate for galaxies that meet the selection criteria is 60%.

The DEIMOS spectroscopy was obtained using the 1200 line/mm grating, with a resolution $R \sim 5000$ covering the wavelength range $6500 - 9100 \text{ \AA}$. Redshifts were measured through an automatic method comparing templates to data, and we only utilise those redshifts measured when two or more lines were identified, providing very secure measurements. Roughly 70% of all targeted objects result in secure redshifts. Most of the redshift failures are galaxies at higher redshift, $z > 1.5$ (Steidel et al. 2004), where the [OII] $\lambda 3727$ line leaves the optical window.

The ACS imaging over the EGS field covers a $10.1' \times 70.5'$ strip, for a coverage area of 0.2 deg^2 . This ACS imaging is discussed in Lotz et al. (2006), and is briefly described here. The imaging consists of 63 tiles imaged in both the F606W (V) and F814W (I) bands. The $5\text{-}\sigma$ depths reached in these images are $V = 26.23$ (AB) and $I = 27.52$ (AB) for point sources, and about two magnitudes brighter for extended objects.

We further utilise Spitzer MIPS $24\mu\text{m}$ imaging, and Chandra X-ray imaging of the EGS field (Nandra et al. 2007) to determine the star forming and AGN properties of our sample. The MIPS $24\mu\text{m}$ imaging is part of the IRAC team GTO program (Papovich et al. 2004). Our procedure was to use a catalog of $24\mu\text{m}$ sources matched to our list of massive galaxies within $1''$, and brighter than $f_{24\mu\text{m}} = 60 \mu\text{Jy}$. This ensures that the source matching is reliable, and that the MIPS detections are significant to $> 3 \sigma$ confidence. We then convert these $24\mu\text{m}$ fluxes into total infrared fluxes utilising the fact that there is a good correlation between fluxes at $15\mu\text{m}$ and the total IR flux (Le Floc'h et al. 2005). We use various templates to convert our observed $24\mu\text{m}$ flux into a total IR flux, from which we compute star formation rates (§4.4.2).

Our matching procedures for these catalogs progressed in the manner described in Bundy et al. (2006) with the K-band catalog serving as our reference. We then match the optical catalogs and spectroscopic catalogs to the K-band catalog, after correcting for astrometry by referencing all

systems to 2MASS stars. The MIPS catalogs and X-rays catalogs are likewise matched in a similar manner.

2.1 Photometric Errors and Detection

We estimate photometric errors, and the K-band detection limit of each K-band image by randomly inserting fake objects of known magnitude, surface brightness profile, and size into each image, and then recovering these simulated objects with the same detection parameters used for real objects. The most basic simulations we perform are done by simply inserting objects with Gaussian profiles with a FWHM of $1''.3$ to approximate the shape of slightly extended, distant galaxies. We then retrieve these objects using the same SExtractor parameters used for the original galaxy detections. We use these simulated retrievals to determine the upper limit completeness of our sample, as well as constrain errors on our photometric measurements. Actual galaxy profiles however have extended envelopes that could be more difficult to measure accurately than compact Gaussian profiles (e.g., Graham et al. 2005).

To determine the detection and photometric fidelity of our images in more detail, we create two sets of 10,000 mock galaxies, each with an intrinsic exponential and de Vaucouleurs profile. These simulated galaxies have properties which are uniformly distributed as follows: K_s band total magnitudes between 15.5 and 20.5 mag, effective radius R_e between 0.0625 and 3.75 arcsec (equivalent to 0.5-30 kpc at $z \sim 1$), and ellipticities between 0 and 0.8. These simulated sources are placed randomly on our Palomar images, and extracted in the same manner as the real source detections. We construct from these simulations detection maps that reveal the fraction of input artificial sources detected per input magnitude and input \log (re) bin (see Figure 1). As expected, galaxies with a de Vaucouleurs profile, which are more centrally concentrated, are easier to detect at a given magnitude. Note that the detection fractions plotted in Figure 1 are independent of output magnitude and size, and are plotted based on their input parameters.

We also estimated systematic errors in measuring magnitudes due to our detection method by using the same simulations (see Figure 2). To do this, we compute the magnitude difference between the recovered and input sources within the input magnitude and size bin. To estimate the output magnitudes, we use exactly the same methods used to find and measure photometry of our actual galaxies. The decreased surface brightness of objects, at a given input magnitude, results in output magnitudes systematically fainter at larger effective radii. In particular, due to the larger tail of the de Vaucouleurs profiles, at a given magnitude and size, the difference in magnitude is larger for the de Vaucouleurs profiles than for the exponential models. At the range of sizes for our sample objects, which range from $0.3''$ - $0.7''$ (Trujillo et al. 2007, submitted), we find that the magnitude and recovery fraction are essential 100% of their simulated value. Depending on the sizes of our galaxies, we could be missing as much as 0.2 mag in the recovered K-band light. We will address this in more detail in §4.2.1.

3 METHODS

We utilise several methods to study the properties of our K-band selected, stellar mass limited sample. The outline of the procedure is described below. The first step in this process, after reducing the K-band imaging, is to create K-selected catalogs. We make these catalogs using SExtractor, optimised for detection and splitting, with both topics discussed in Bundy et al. (2006, 2007). We then utilise the K-band imaging, combined with the optical imaging, to compute stellar masses from which our sample is selected. We then match these massive galaxies to MIPS, X-ray and Hubble sources from which we derive the physical features, and the evolution of these systems.

3.1 K-band Selection

Within the total K-band area of our survey (1.53 deg^2) we detect 61,489 sources, after removing false artifacts. Most of these objects (92%) are at $K < 21$, while 68% are at $K < 20$, and 37% are at $K < 19$. In total there are 38,613 objects fainter than $K = 19$ in our sample. Out of our total K-band population, 10,693 objects have secure spectroscopic redshifts from the DEEP2 redshift survey (Davis et al. 2003). We supplement these by 37,644 photometric redshifts within the range $0 < z < 2$ (§3.2).

Because our spectroscopy is R-band selected, while our stellar masses are based on K-band detections, we are required to divided our sample into different sub-samples. We construct a “primary sample” consisting of those galaxies with both spectroscopic redshifts and K-band detections. By construction, these galaxies also have optical magnitudes $R_{AB} < 24.1$. The matching between our K-band catalogue, and the DEEP2 catalogue was done with a $1''$ tolerance. This results in a very low spurious rate of 1-2% due to the low surface densities in both catalogues. Most of the galaxies with spectroscopic redshifts are detected in the K-band, at a rate between 65-90%, depending on the K-band depth. Because we are interested in the most massive galaxies, which appear bright in the NIR, the present study is not biased by these non-matches.

The “secondary” sample consists of those galaxies with photometric redshifts. Within the secondary sample, there are two kinds of photometric redshifts. The first are those systems which have optical magnitudes at $R_{AB} < 24.1$, the limit for spectroscopy. The other types of photometric redshifts are for those galaxies which have optical magnitudes fainter than this optical limit, in which we use a different method to compute photometric redshifts (§3.2). This second set includes all galaxies at $z > 1.4$, which have purely photometrically measured redshifts.

3.2 Photometric Redshifts

We calculate photometric redshifts for our K-selected galaxies which do not have DEEP2 spectroscopy. This sample is referred to as the photometric-redshift or secondary sample. These photometric redshifts are based on the optical+near infrared imaging, in the BRIJK (or BRIK for half the sample) bands, and are fit in two ways, depending on the brightness of a galaxy in the optical. For galaxies that meet the

spectroscopic criteria, $R_{AB} < 24.1$, we utilise a neural network photometric redshift technique to take advantage of the vast number of secure redshifts with similar photometric data. Most of the $R_{AB} < 24.1$ sources not targeted for spectroscopy should be within our redshift range of interest, at $z < 1.4$. The neural network fitting is done through the use of the ANNz (Collister & Lahav 2004) method and code. To train the code, we use the ~ 5000 redshifts in the EGS, which has galaxies spanning our entire redshift range. The training of the photometric redshift fitting was in fact only done using the EGS field, whose galaxies are nearly completed selected based on the magnitude limit of $R_{AB} < 24.1$. We then use this training to calculate the photometric redshifts for galaxies with $R_{AB} < 24.1$ in all fields. The overall agreement between our photometric redshifts and our ANNz spectroscopic redshifts is very good using this technique, with $\delta z/(1+z) = 0.07$ out to $z \sim 1.4$. The agreement is even better for the $M_* > 10^{11} M_\odot$ galaxies where we find $\delta z/(1+z) = 0.025$ across all of our four fields. The photometry we use for our photometric redshift measurements are done with a $2''$ diameter aperture.

For galaxies which are fainter than $R_{AB} = 24.1$ we utilise photometric redshifts using Bayesian techniques, and the software from Benitez (2000). For an object to have a photometric redshift we require that it be detected at the 3σ level in all optical and near-infrared (BRIJK) bands, which in the R-band reaches $R_{AB} \sim 25.1$ (Coil et al 2004b). We optimised our results, and corrected for systematics, through the comparison with spectroscopic redshifts, resulting in a redshift accuracy of $\delta z/z = 0.17$ for $R_{AB} > 24.1$ systems. These $R_{AB} > 24.1$ galaxies are however only a very small part of our sample. Up to $z \sim 1.4$ only 6 (2.6%) of our $M_* > 10^{11.5} M_\odot$ galaxies are in this regime, while 412 $10^{11} M_\odot < M_* < 10^{11.5} M_\odot$ (9%) of our galaxies have an R-band magnitude this faint. All of these systems are furthermore at $z > 1$. At $z > 1.4$ all of our sample galaxies are measured through the Benitez (2000) method due to a lack of training redshifts. There are instances where not all galaxies are detected in the optical bands, and the way we deal with these galaxies is discussed in §4.2.1 in terms of our measured number and mass densities.

One concern with utilising the DEEP2 spectroscopy as the prior in the ANNz method is that any galaxies which are actually at higher redshifts, but with $R_{AB} < 24.1$, could contain a very incorrect redshift. This is particularly important in this paper, as we do not wish to have additional galaxies added to our sample which could produce false artifacts in the number and mass density evolution, as well as incorrect identifications of massive galaxies. We know that about 30% of galaxies with $R_{AB} < 24.1$ will be at $z > 1.4$ (Steidel et al. 2004). These systems at $z > 1.4$ are however nearly all fainter than $K = 20$ (Reddy et al. 2006), and are thus not likely contaminating our massive galaxy sample, which is nearly all at $K < 19$.

After our photometric redshifts were calculated, the CFHT legacy survey published their own independent photometric redshifts in the EGS, which are on average within $\delta z/(1+z) = 0.2$ of our photometric redshifts. The poorer agreement between the CFHT legacy survey photometric redshifts and ours is likely due to the lack of NIR data in the CFHT fits, and the more restrictive priors used in the CFHT photometric redshift fitting (cf. Bundy et al. 2006).

In any case, we do not use individual photometric redshifts, and only utilise them in large ensembles, where errors due to photometric redshift mismatches can be properly accounted for.

3.3 Stellar Masses

We match our K-band selected catalogs to the CFHT optical data to obtain spectral energy distributions (SEDs) for all of our sources, resulting in measured BRIJK magnitudes. From these we compute stellar masses based on the methods and results outlined in Bundy, Ellis, Conselice (2005) and Bundy et al. (2006). Stellar masses computed in this way have a long established history (e.g., Sawicki & Yee 1998). About 40% of our sample do not contain J-band imaging, but the stellar masses computed do not vary significantly when the J-band data is included or excluded. All our stellar masses are furthermore normalised by the observed rest-frame K-band light, which is roughly at rest-frame $\sim 1\mu m$ for most galaxies.

The basic mass fitting method consists of fitting a grid of model SEDs constructed from Bruzual & Charlot (2003) (BC03) stellar population synthesis models, with different star formation histories. We use an exponentially declining model to characterise the star formation history, with various ages, metallicities and dust contents included. These models are parameterised by an age, and an e-folding time for parameterising the star formation history, where $SFR \propto e^{-t/\tau}$. The values of τ are randomly selected from a range between 0.01 and 10 Gyr, while the age of the onset of star formation ranges from 0 to 10 Gyr. The metallicity ranges from 0.0001 to 0.05 (BC03), and the dust content is parametrised by τ_V , the effective V-band optical depth for which we use values $\tau_V = 0.0, 0.5, 1, 2$. Although we vary several parameters, the resulting stellar masses from our fits do not depend strongly on the various selection criteria used to characterise the age and the metallicity of the stellar population.

It is however important to realise that these parameterisations are fairly simple, and it remains possible that stellar mass from older stars is missed under brighter, younger, populations. While the majority of our systems are passively evolving older stellar populations, it is possible that up to a factor of two in stellar mass is missed in any star bursting blue systems. However, stellar masses measured through our technique are roughly the expected factor of 5-10 smaller than dynamical masses at $z \sim 1$ using a sample of disk galaxies (Conselice et al. 2005b), demonstrating their inherent reliability.

We match magnitudes derived from these model star formation histories to the actual data to obtain a measurement of stellar mass using a Bayesian approach. We calculate the likely stellar mass, age, and absolute magnitudes for each galaxy at all star formation histories, and determine stellar masses based on this distribution. Distributions with larger ranges of stellar masses have larger resulting uncertainties. It turns out that while parameters such as the age, e-folding time, metallicity, etc. are not likely accurately fit through these calculations due to various degeneracies, the stellar mass is robust. Typical errors for our stellar masses are 0.2 dex from the width of the probability distributions. There are also uncertainties from the choice of the IMF.

Our stellar masses utilise the Chabrier (2003) IMF, which can be converted to Salpeter IMF stellar masses by adding 0.25 dex. There are additional random uncertainties due to photometric errors. The resulting stellar masses thus have a total random error of 0.2-0.3 dex, roughly a factor of two. The details behind these mass measurements and their uncertainties is also described in papers such as Brinchmann & Ellis (2000), Papovich et al. (2006) and Bundy et al. (2006).

There is furthermore the issue of whether or not our stellar masses are overestimated based on using the Bruzual & Charlot (2003) models. It has recently been argued by Maraston (2005) and Bruzual (2007) that a refined treatment of thermal-pulsating AGB stars in the BC03 models results in calculated stellar masses that can be too high by a factor of a few. While we consider an uncertainty of a factor of two in our stellar masses, it is worth investigating whether or not our sample is in the regime where the effects of a different treatment of TP-AGB stars in e.g., Maraston (2007) will influence our mass measurements. This has been investigated recently in Maraston (2005) and Bruzual (2007) who have both concluded that galaxy stellar masses computed with an improved treatment of TP-AGB stars are roughly 50-60% lower.

This problem has also been recently investigated independently by Kannappan & Gawiser (2007) who come to similar conclusions, but do not advocate one model over another. Furthermore, the effect of TP-AGB stars is less important at our rest-frame wavelengths probed than at longer wavelengths, especially in the rest-frame IR. Our survey is K-selected, and the observed K-band is used as the flux in which the masses are computed. The rest-frame wavelength probed with the observed K-band ranges from $0.7\mu\text{m}$ to $1.5\mu\text{m}$ where the effects of TP-AGB stars are minimised. The ages of our galaxies are also older than the ages where TP-AGB stars have their most effect (Maraston 2005; Bruzual 2007). To test this, after our analysis was finished, we utilised the newer Bruzual and Charlot (2007, in prep) models, which include a new TP-AGB star prescription, on our massive galaxy sample. From this we find on average a ~ 0.07 dex smaller stellar mass using the newer models. At most, the influence of TP-AGB stars will decrease our stellar masses by 20%. The effect of this would decrease the number of galaxies within our sample, particularly those close to the $M_* = 10^{11} M_\odot$ boundary. This systematic error is however much smaller than both the stellar mass error we assume (0.3 dex), and the cosmic variance uncertainties, and thus we conclude it is not a significant factor.

4 THE PROPERTIES AND EVOLUTION OF MASSIVE GALAXIES

4.1 Sample Selection

Our K-band selection allows us to measure the stellar masses of galaxies to $K \sim 20 - 21$. The stellar mass function for galaxies within these limits is discussed in Bundy et al. (2006) for our sample. In this paper we discuss only those galaxies with $M_* > 10^{11} M_\odot$. The K-band magnitude distribution with redshift and the stellar mass distribution with redshift are shown in Figure 3. Figure 3 displays our total sample - consisting of the primary spectroscopic, and

secondary photometric redshift selected galaxies combined. While the selection limit of $M_* = 10^{11} M_\odot$ is somewhat arbitrary, it is however the mass limit in which we are reasonably completed out to $z \sim 2$.

Figure 3a shows the K-band magnitude distribution for our sample, demonstrating that all of our sample is at $K < 20$, where we are 100% complete in K-band detections (§2.1; Conselice et al. 2007b). However, we are not complete in other bands at all redshifts for a $K < 20$, and thus a $M_* > 10^{11} M_\odot$ selected sample. At $R_{\text{AB}} = 25.1$ we are complete at $10^{10.5} M_\odot < M_* < 10^{11} M_\odot$ up to $z \sim 1$, up to $z \sim 1.4$ for $10^{11} M_\odot < M_* < 10^{11.5} M_\odot$, and up to $z \sim 2$ for $M_* > 10^{11.5} M_\odot$. However, this completeness is not the same in the B-band. This needs to be accounted for as we do not include photometric redshifts measurements for galaxies which are undetected in one of our bands (§3.2). However, for the redshift and mass ranges plotted in Figure 3 & 4 and listed in Table 2, we are 100% complete at $z < 1.2$ and are 2% - 10% incomplete at higher redshifts. The method we use to calculate, and correct for, this incompleteness in the number and mass densities is discussed in §4.2.1.

Utilising our stellar mass catalogs, the selection of massive galaxies out to $z \sim 2$ is straightforward, and is simply a cut at stellar masses $M_* > 10^{11.5} M_\odot$ and $M_* > 10^{11} M_\odot$. We do not consider lower mass galaxies in this analysis, due to significant incompleteness, although these galaxies may show the most evolution within these redshifts, as can be seen in the star formation downsizing (e.g., Bundy et al. 2006). In this paper, galaxies with masses $M_* < 10^{11} M_\odot$ are only discussed in terms of their relationship to higher mass galaxies. Note that our massive galaxies are much brighter than the survey 5σ limit of $K = 20.5 - 21$. As Figure 3 shows, we are unlikely missing galaxies within our mass selection which are fainter than this limit up to $z \sim 2$ (§4.2.1). For example, at $z \sim 1.5 - 2$ galaxies with a maximum M/L ratio with $M_* = 10^{11} M_\odot$ would still be several times brighter than our K-limit.

4.2 Number Densities of Massive Galaxies

In this section we examine in detail the number density and mass density evolution for massive galaxies found between $z \sim 0$ and $z \sim 2$. For the purposes of this paper we consider galaxies with $M_* > 10^{11} M_\odot$ as massive systems. These galaxies are in fact the most massive galaxies in the nearby universe, and are generally not found in smaller area NIR surveys. For example, in the Hubble Deep Field-North (HDF-N), there are only four galaxies with stellar masses $M_* > 10^{11} M_\odot$, and none with $M_* > 10^{11.5} M_\odot$ (Dickinson et al. 2003) using a Chabrier IMF. In comparison, we have 4571 galaxies with $M_* > 10^{11} M_\odot$, and 225 galaxies with $M_* > 10^{11.5} M_\odot$ up to $z \sim 1.4$. Although the HDF-N might be slightly depleted of massive galaxies, it shows the importance of using a large area survey to determine the properties and evolution of massive galaxies. Roughly 30% of our $M_* > 10^{11} M_\odot$ galaxies have measured spectroscopic redshifts, while 36% of the $M_* > 10^{11.5} M_\odot$ galaxies have spectroscopic redshifts. We show the redshift distribution of our sample of galaxies as a function of redshift up to $z \sim 2$ as a function of mass and K-band magnitude in Figure 3, with the massive galaxies with masses $10^{11} M_\odot < M_* < 10^{11.5} M_\odot$, and $M_* > 10^{11.5} M_\odot$ labelled.

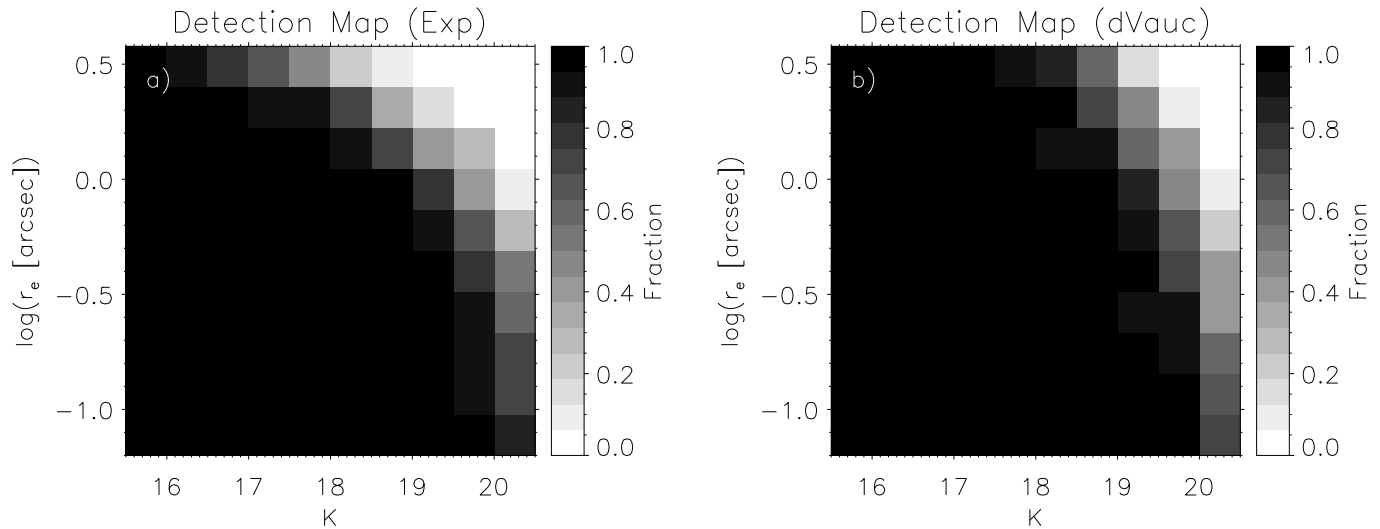


Figure 1. a) Detection map for simulated sources with exponential profiles placed at random in our Ks band images. The gray-scale map reflects the ratio between input and recovered objects per input magnitude and $\log(r_e)$ bin. b) Same as a) but showing the detection map for simulated sources with a de Vaucouleurs profiles.

Table 2. Galaxy Number and Mass Density Evolution and Star Formation Rates as a Function of Mass

Mass	Redshift	$\log(\phi)$ ($h_0^3 \text{ Mpc}^{-3} \text{ dex}^{-1}$)	$\log(\rho)$ ($h_0^3 \text{ M}_\odot \text{ Mpc}^{-3}$)	$\log \rho_{\text{SFR}}$ ($\text{M}_\odot h_0^3 \text{ yr}^{-1} \text{ Mpc}^{-3}$)
$\log M_* > 11.5$	0.5	$-4.62^{+0.51}_{-0.26}$	$6.83^{+0.49}_{-0.24}$	$-4.9^{+0.2}_{-0.3}$
	0.7	$-4.29^{+0.32}_{-0.21}$	$7.17^{+0.28}_{-0.21}$	$-3.6^{+0.2}_{-0.3}$
	0.9	$-4.08^{+0.23}_{-0.20}$	$7.34^{+0.28}_{-0.20}$	$-3.0^{+0.2}_{-0.3}$
	1.1	$-4.28^{+0.30}_{-0.20}$	$7.10^{+0.29}_{-0.20}$	$-2.9^{+0.2}_{-0.3}$
	1.3	$-5.05^{+0.45}_{-0.29}$	$6.73^{+0.24}_{-0.21}$	$-3.3^{+0.2}_{-0.3}$
	1.5	$-4.91^{+0.26}_{-0.22}$	$6.83^{+0.14}_{-0.21}$...
	1.7	$-5.03^{+0.22}_{-0.22}$	$6.66^{+0.17}_{-0.22}$...
	1.9	$-5.33^{+0.25}_{-0.25}$	$6.36^{+0.16}_{-0.25}$...
$11 < \log M_* < 11.5$	0.5	$-3.32^{+0.10}_{-0.11}$	$7.76^{+0.11}_{-0.11}$	$-2.6^{+0.2}_{-0.3}$
	0.7	$-3.21^{+0.09}_{-0.10}$	$7.79^{+0.10}_{-0.11}$	$-2.2^{+0.2}_{-0.3}$
	0.9	$-3.08^{+0.08}_{-0.10}$	$7.92^{+0.09}_{-0.10}$	$-2.0^{+0.2}_{-0.3}$
	1.1	$-3.26^{+0.09}_{-0.10}$	$7.83^{+0.09}_{-0.10}$	$-1.9^{+0.2}_{-0.3}$
	1.3	$-3.66^{+0.09}_{-0.10}$	$7.44^{+0.08}_{-0.11}$	$-2.1^{+0.2}_{-0.3}$
	1.5	$-3.80^{+0.09}_{-0.11}$	$7.42^{+0.10}_{-0.11}$...
	1.7	$-4.10^{+0.11}_{-0.11}$	$7.11^{+0.11}_{-0.11}$...
$10.5 < \log M_* < 11$	0.5	$-2.80^{+0.06}_{-0.07}$	$7.88^{+0.06}_{-0.07}$...
	0.7	$-2.80^{+0.06}_{-0.07}$	$7.88^{+0.06}_{-0.07}$...
	0.9	$-2.69^{+0.12}_{-0.07}$	$7.79^{+0.06}_{-0.07}$...

The fact that such massive galaxies exist at high redshift is not completely surprising, as a large number of massive galaxies have been found at $z \sim 1.5 - 2$, albeit in much smaller fields (Glazebrook et al. 2004; Saracco et al. 2005). Cosmic variance is an issue in these previous studies, which have areas over a factor of ten smaller than ours. This is especially a problem, even within our survey, for the most massive galaxies, which are the most clustered within the redshift ranges we examine (e.g., Coil et al. 2004a; Foucaud et al. 2007). As a result, these massive $M_* > 10^{11.5} \text{ M}_\odot$ galaxies are nearly completely absent in previous high

redshift stellar mass studies, although a few examples exist in some previous work using smaller area fields.

4.2.1 Sources of Uncertainty and Redshift Completeness

Because any variations in number or mass densities suggest evolution, it is important to consider the various errors that can mimic real evolution in our analysis both in terms of evolution in number/mass densities, as well as for the selection of the most massive galaxy sample which we examine later in the paper. Beyond random and shot noise errors, we also consider stellar mass measurement errors, both systematic

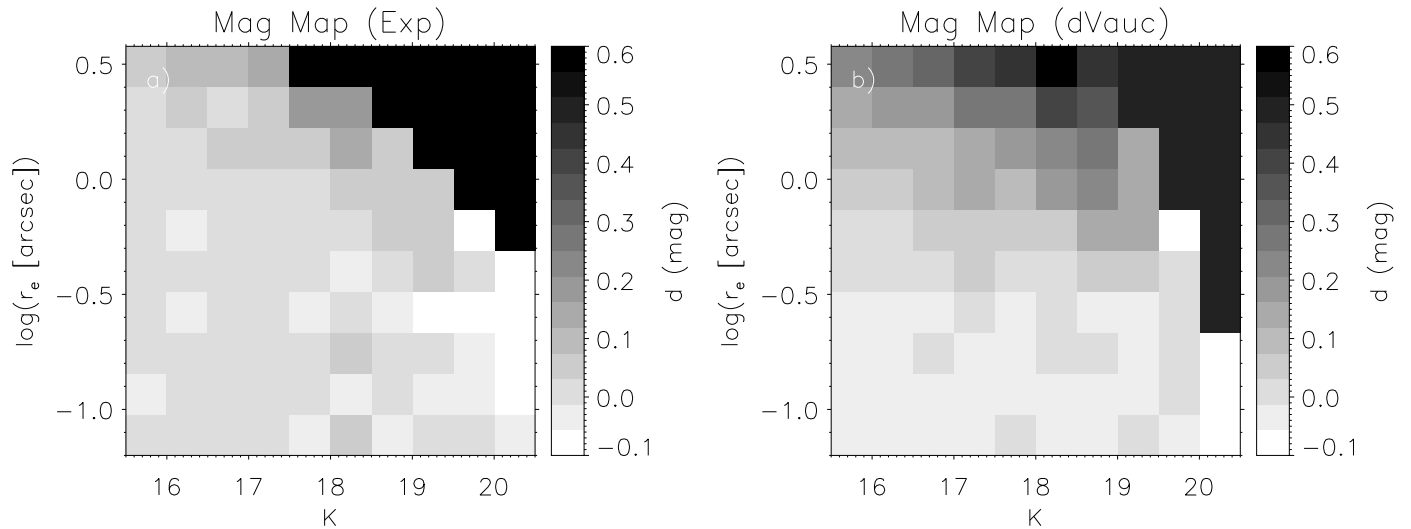


Figure 2. a) Magnitude map for simulated sources with exponential profiles placed at random in our Ks band images. The gray-scale map reflects the difference between input and recovered magnitudes per input magnitude and $\log(r_e)$ bin. b) Same as a) but showing the magnitude map for simulated sources with a de Vaucouleurs profiles.

and random, as well as errors from cosmic variance when examining the evolution of galaxy number and mass densities. This includes considering in the stellar mass errors issues with photometry, both random and systematic. We also consider in our stellar mass density and number density measurements the errors produced through using photometric redshifts. We do this through Monte-Carlo simulations of how the stellar mass function would change given the known uncertainty on these measurements. This also gives us some idea of the Eddington bias which is affecting our selection near the $M_* = 10^{11} M_\odot$ and $M_* = 10^{11.5} M_\odot$ boundary selection limits.

The random errors result from Poisson statistics on the number of galaxies (N) in each redshift and mass bin. We thus include a component in our error budget to account for these counting uncertainties. Stellar mass uncertainties are considered in two ways. The first method uses Monte-Carlo simulations of mass errors to calculate how a typical 0.3 dex error can affect the measurement of number densities. This is the typical error due to mismeasuring the stellar masses for our sample (e.g., Bundy et al. 2006). This factor of two comes from several sources, which we conclude are all contributing random errors to our mass budget. Below we examine the reasoning for this, and why we do not include any systematic stellar mass uncertainties.

It is first important to note that our photometry originates from SExtractor, and does not use the *imcat* software utilised by DEEP2 to obtain photometry for target selection and luminosity functions (e.g, Faber et al. 2005). We investigated systematic issues in the photometry through our simulations of placing fake galaxies of known magnitude into our images, and then determining how the detected magnitude differs from the input. We found that when the completeness was high, the retrieved magnitude was almost nearly identical to the input. The completeness at $K \sim 20$, the faintest magnitude where our galaxies are found, is $\sim 100\%$ (§2.1), and we are thus unlikely affected by a systematic

photometry error. We do not include any additional systematic uncertainty into our error budget due to our detection methods.

We also compare our total SExtractor MAGAUTO magnitudes to magnitudes measured using $4''$ diameter aperture photometry, and find a very slight change with redshift, such that we are not detecting all the light in the highest redshift galaxies using total magnitudes. This however is a very slight effect, with at most a difference of 0.03 mag which corresponds to 0.01 dex in stellar mass. Again, however, this effect is less of an issue for the brightest galaxies, which are the dominate population in our sample.

We conclude that the factor of two, or 0.3 dex random uncertainty in the stellar mass is a representative estimate of the uncertainties in stellar masses. To determine how a 0.3 dex random error in stellar masses can change our densities, we simulate how the mass function and number densities of our sample would change after applying this error. We do this by changing the measured stellar masses by a random amount, to within 0.3 dex, and then recalculate the number and mass densities. The difference in stellar mass and number densities between the recomputed and original values is then added to the error budget.

Another major source of error in our number densities originates from cosmic variance. Based on the likely bias (b) and dark matter variance (σ_{DM}), it is possible to calculate the likely cosmic variance (Somerville et al. 2004), and to include this in our error budget. For massive galaxies with $M_* > 10^{11} M_\odot$, and using the volume of our survey within each redshift bin, we calculate that the galaxy variance is $\sim 0.3 - 0.5$. This leads to a fractional variation of 20-30% for the most massive galaxies. This variance drops by a factor of three for the lower mass galaxies in our sample, rendering cosmic variance less of an issue for these systems. When we consider our four fields, which are widely separated, it reduces the estimates of our cosmic variance by a factor of two. It turns out that our computed number and mass densi-

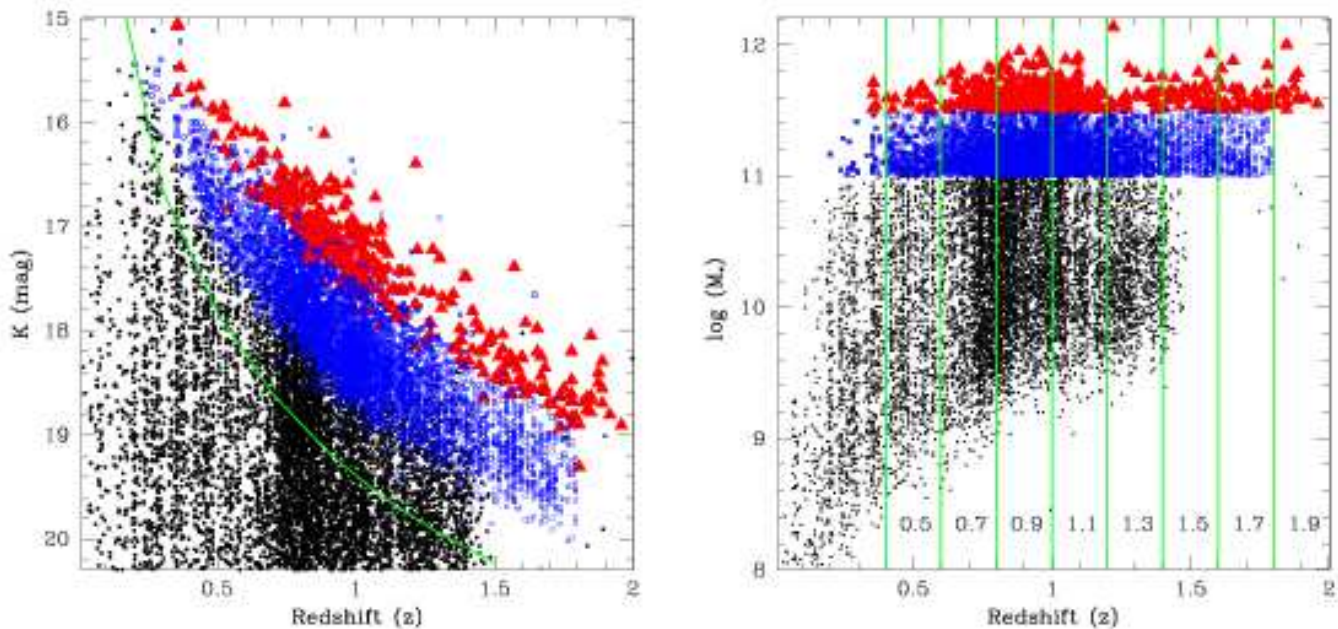


Figure 3. Left panel: the K magnitude vs. redshift (z) diagram for our total $z < 2$ sample with spectroscopic and photometric redshifts combined. The red triangles show the locations of galaxies with derived stellar masses $M_* > 10^{11.5} M_\odot$, and the blue boxes show the location of galaxies with $10^{11} M_\odot < M_* < 10^{11.5} M_\odot$. The solid green line shows the evolution of L^* in the K-band out to $z \sim 1.5$ based on the results of Drory et al. (2004). Right panel: the stellar mass distribution as a function of redshift. As in the left panel, the red triangles are galaxies with $M_* > 10^{11.5} M_\odot$, and the blue boxes are for galaxies with $10^{11} M_\odot < M_* < 10^{11.5} M_\odot$. The green vertical lines show the location of the bins we use in our analysis of the statistical properties of these massive galaxies, including their number and mass densities. The numbers within each bin label their median redshift. We also include as small points in both panels the K-band magnitude and stellar mass distribution for all galaxies with spectroscopic redshifts at $z < 1.4$.

ties (Table 2) are often dominated by these cosmic variance errors.

Another source of uncertainty is the fact that if a galaxy does not have a measured photometric redshift, it cannot be included in our sample. As discussed in §3.2, we do not measure photometric redshifts for galaxies not detected in one of our optical bands. To investigate whether we could be missing significant numbers of massive galaxies, particularly at high redshift, where we find evolution, we examine the number of galaxies which are not detected in one band, but which could be high redshift massive galaxies. First, as Figure 3 shows, the K-limit for our massive galaxy sample is roughly $K = 19$ for $M_* > 10^{11} M_\odot$ galaxies at redshifts $z < 1.4$. There are only 16 objects in our K-selected sample that are within this K-band magnitude limit, but are not detected in the B-band, and thus do not have a measured photometric redshift. Most of these galaxies are near the K-limit with $K > 18$, and none are as bright as the $M_* > 10^{11.5} M_\odot$ galaxies.

These galaxies with missing optical fluxes are unlikely influencing our measured number and mass densities at $z < 1.2$ for the following reasons. The total number of galaxies with $M_* > 10^{11.5} M_\odot$ at $z \sim 1.4$ is 45. If all 16 galaxies at our K-limit without a photometric redshift were placed into this bin, it would only increase densities by 30%, not enough to account for the non-evolution we see. Furthermore, a $M_* > 10^{11.5} M_\odot$ galaxy with a maximum M/L ratio would still be brighter than $K = 18$ at $z \sim 1.4$, and thus these 16 galaxies are not likely to be at $z < 1.4$ with a mass $M_* >$

$10^{11.5} M_\odot$. The $10^{11} M_\odot < M_* < 10^{11.5} M_\odot$ bin at $z \sim 1.4$ contains 725 galaxies, and these 16 galaxies would contribute a neglectable amount to their number and mass densities at $z \sim 1.4$. We therefore conclude that our criteria that galaxies be detected in all optical bands to be included in our sample is a very insignificant source of uncertainty in our analysis at $z < 1.4$.

We are however less complete for selecting galaxies within our mass ranges at $z > 1.2$. We correct for this by adding the number of galaxies at these higher redshifts that are likely missed. We following Willmer et al. (2005) for this process, where we consider the likely sampling based on the K and I magnitudes, and the (I-K) colour for systems which did not have a measured photometric redshift, and are missing a flux in one of the two other optical bands (generally the B-band). We add into our number and mass densities those objects which have a optical-NIR colour and magnitude in I and K similar to the distribution of real galaxies in the given stellar mass and redshift bin. This will in fact give an upper limit on the density corrections, however in reality it makes little difference to the values.

4.2.2 Number and Mass Density Evolution

One of the most basic methods for understanding the evolution of massive galaxies is determining how their number densities and integrated mass densities change as a function of redshift. In Bundy et al. (2006) we examined the overall change in the number densities of massive galaxies, finding

little apparent evolution when comparing mass functions. We reexamine this in more detail using our spectroscopic plus photometric redshift sample. We furthermore examine this evolution in smaller redshift bins, and explicitly state how the evolution of the mass function is occurring, or not occurring, for the most massive galaxies, and with what certainly we can make such statements.

As we are counting galaxies, as opposed to using the V_{\max} method to calculating mass functions, we differ in our approach from Bundy et al. (2006). It is important to therefore test that our methods give consistent results. We find this is the case using the published Schechter functions in Bundy et al. (2006), derived from V_{\max} computed mass functions, and our method of empirically determining whether there is evolution by counting actual galaxies. We find an agreement between the two methods using the Bundy et al. (2006) redshift bins (0.4-0.7, 0.7-1.0, and 1.0-1.4). In the $M_* > 10^{11.5} M_{\odot}$ mass range we find slightly more galaxies using our counting method. This is due to the Schechter function under-fitting the high mass end in Bundy et al. (2006), something that also occurs for the $z = 0$ mass function fits (see below).

Figure 4 shows the number and mass density evolution of the combined primary spectroscopic, and secondary photometric-redshift selected, galaxies for systems with masses $M_* > 10^{11.5} M_{\odot}$ and $10^{11} M_{\odot} < M_* < 10^{11.5} M_{\odot}$ out to $z \sim 2$. Also included is the evolution in number densities for galaxies with masses $10^{10.5} M_{\odot} < M_* < 10^{11} M_{\odot}$. We show the number densities of galaxies within these mass ranges measured in the nearby universe out to $z \sim 0.2$ by the 2MASS/2dF galaxy surveys (Cole et al. 2001) normalised using the same Chabrier IMF as we use for our higher redshift comparisons.

It is clear by looking at Figure 4, and analysing the number densities listed in Table 2, that there is very little evolution, statistically, at $z < 1$ for the $M_* > 10^{10.5} M_{\odot}$ systems. We can conclude that all massive $M_* > 10^{11.5} M_{\odot}$ galaxies are present by $z \sim 1$ to within a factor of 2-3 (see e.g., Cimatti et al. 2006; Bundy et al. 2006; Brown et al. 2007). However, as can be seen in Figure 4 there is some evolution for these massive galaxies at $z > 1$, with evolution occurring up to $z \sim 1.5$ as well as up to $z \sim 2$. This is the first time that a study has had a large enough area to make this claim, and as we argue below, at least a fraction of the increase in total stellar mass seen between $z \sim 1$ and $z \sim 2$ (e.g., Dickinson et al. 2003) is produced in massive galaxies.

As can be seen by eye, within our observational errors, there is some evolution in number densities for $M_* > 10^{11} M_{\odot}$ and perhaps $M_* > 10^{11.5} M_{\odot}$ selected galaxies between $z \sim 1-1.5$, although it is not clear with a casual examination whether this is significant. The evolution in the number and mass densities can be examined quantitatively in a number of ways. First, when we consider evolution just within our sample from $z = 1.5$ to $z = 1$ we find significant increases at masses $M_* < 10^{11.5} M_{\odot}$, both in terms of number and mass densities. We describe below a quantitative analysis of these changes.

Galaxies with stellar masses $M_* > 10^{11.5} M_{\odot}$ show an increase in number densities between $z = 1.5$ to 0.4 of a factor of $2.7^{+1.8}_{-1.7}$. This is however significant only at the $< 2\sigma$ level, considering all uncertainties. In fact, all of this apparent evolution occurs at $z > 1$. Furthermore, we find a

factor of $1.3^{+0.74}_{-0.53}$ increase in the mass density associated with $M_* > 10^{11.5} M_{\odot}$ galaxies at the same redshift range, although this is also at less than 3σ significance. When we investigate evolution from $z \sim 2$ to $z \sim 1$ we find an increase of $11.2^{+8.7}_{-4.9}$ in number densities, and a factor of $5.5^{+4.3}_{-1.7}$ increase in mass densities for systems with $M_* > 10^{11.5} M_{\odot}$. This is also an insignificant increase, and it appears that for the most part galaxies with $M_* > 10^{11.5} M_{\odot}$ are nearly all formed by $z \sim 2$. We cannot however rule out a factor of 2-3 evolution in number densities for these galaxies, given our large uncertainties.

We calculate the evolution for $M_* > 10^{11.5} M_{\odot}$ galaxies down to $z \sim 0$ by comparing with nearby galaxy studies, such as Cole et al. (2001). It is important to note however that these local studies were done using different techniques than ours, and there is potentially significant systematic differences used to measure the total amount of light in these nearby galaxies, and in the way the stellar mass was computed. The largest difference is that the 2MASS data used to calculate the stellar masses in Cole et al. (2001) may under-represent the total amount of light, given its shallow depth, by up to 0.5 mags. As we are potentially also missing light in our massive galaxies (§2.1), a direct comparison between our data and Cole et al. (2001) is fair, although a systematic difference of a few 10%-s of percentage cannot be ruled out.

Through a direct comparison with Cole et al. (2001) there is a factor of $2.2^{+1.5}_{-1.4}$ increase in number density, and a factor of $0.74^{+0.46}_{-0.31}$ increase in integrated stellar mass between $z \sim 1.5$ and $z \sim 0$ for $M_* > 10^{11.5} M_{\odot}$ systems. These $z \sim 0$ number and mass densities are taken from the Schechter fits and data presented in Cole et al. (2001). Note that the Cole et al. (2001) Schechter function under-fits the most massive systems. We correct this by explicitly using the number densities for the most massive galaxies tabulated in Cole et al. (2001).

Galaxies with stellar masses $10^{11} M_{\odot} < M_* < 10^{11.5} M_{\odot}$ show significant evolution in number density. The number densities of systems with $10^{11} M_{\odot} < M_* < 10^{11.5} M_{\odot}$ increases by a factor of $2.2^{+0.57}_{-0.41}$ between $z = 1.4$ and $z = 0.4$, a result significant at $> 4\sigma$. Just as for the most massive systems, this evolution occurs completely at $z > 1$. Similarly, we find a factor of $2.1^{+0.6}_{-0.35}$ increase in the integrated mass density for systems with $10^{11} M_{\odot} < M_* < 10^{11.5} M_{\odot}$ within the same redshift range, also at $> 4\sigma$ confidence. We find furthermore, after correcting for incompleteness due to the R-band limit (§4.2.1), that there is a factor of $14.5^{+4.1}_{-2.8}$ evolution in the number densities, and a factor of $10.7^{+3.1}_{-2.0}$ in mass densities between $z \sim 2$ and $z \sim 1$ for galaxies with $10^{11} M_{\odot} < M_* < 10^{11.5} M_{\odot}$. Both of these are significant at the 5σ level. When we consider evolution from $z \sim 1.5$ to $z \sim 0$, using the comparison to Cole et al. (2001), we find a factor of $3.0^{+0.78}_{-0.56}$ increase in number densities, and an increase of $1.7^{+0.49}_{-0.29}$ in mass densities. Both of these increases are significant at the $> 5\sigma$ level.

These results show that there is some evolution in the number and mass densities of massive galaxies at $z \sim 1-2$. This evolution is such that the most massive systems with $10^{11} M_{\odot} < M_* < 10^{11.5} M_{\odot}$ increase in number and mass densities by factors $> 2-3$ at a significance $> 3\sigma$. Taken as a whole, we calculate that the scenario whereby the stellar mass and number densities of galaxies does not evolve between $z \sim 1.5$ to $z \sim 0.4$ can be rejected at $> 8\sigma$ confi-

dence. Therefore it does not appear that high mass galaxy formation, with the exception of $M_* > 10^{11.5} M_\odot$ systems, is complete by $z \sim 1.4$, yet it is largely completed by $z \sim 1$. Therefore, the redshift range $z \sim 1 - 1.5$ is the final epoch for the build up of the majority of the stellar mass in the most massive galaxies.

4.2.3 Mass Function Peak

As can be seen in Figure 4, galaxies with $M_* > 10^{11.5} M_\odot$ have perhaps a surprisingly higher galaxy number and mass density at $z \sim 1$ than at $z \sim 0.4$. This is unlikely a volume effect, as the total co-moving volume of our sample at $z \sim 0.9$ is $2.4 \times 10^6 \text{ Mpc}^3$, while at $z \sim 0$ the 2dF/2MASS sample occupies $5 \times 10^6 \text{ Mpc}^3$ (Cole et al. 2001). The other redshift bins have similar co-moving volumes as the $z \sim 0.9$ bin. Furthermore, we can see this over-density, to a much lesser degree, in the number and mass densities using other mass cuts.

Due to the photometric selection there are more galaxies at $z > 0.7$ with spectroscopic redshifts than at lower redshifts. This should not however create such a difference, as we are filling in the missing galaxies using photometric redshifts. To test whether this effect is due to the spectroscopic redshifts picking up at $z > 0.7$, we redo Figure 4 using just photometric redshifts. When we do so, we obtain nearly the same result (Figure 4). We also see this peak to a limited degree when only examining objects with spectroscopic redshifts.

Another issue is whether the photometric redshifts, most of which were trained with a neural network method (ANNz), are somehow biased towards a $z \sim 0.9$ redshift. We tested this in a number of ways. First, the spike at $z \sim 0.9$ for the $M_* > 10^{11.5} M_\odot$ galaxies appears to be dominated by fairly low number statistics, and the peak is most obvious in Field 2. There is perhaps a slight excess in the EGS, but there is no excess or peak seen in Fields 3 or 4 when examining either the photometric or spectroscopic redshifts. Secondly, the ANNz method may bias the fitted redshifts to exist at only certain values. This is likely not occurring in our sample for the following reasons. We are training our method using only the EGS field, which has a spectroscopic over-density at $z = 0.7$, while our over-density is found at $z \sim 0.9$. When we examine the distribution of the number of $M_* > 10^{11} M_\odot$ galaxies as a function of redshift in narrow $\delta z = 0.005$ bins, we do not find any trend or correlation between spectroscopic redshifts and photometric redshifts. That is, the locations in redshift where photometric redshifts are found are not the same as the spectroscopic redshifts.

An increase in number density over the $z \sim 0$ values for massive galaxies can be seen, often to an even greater level, in the mass functions plotted in Bundy et al. (2006), as well as in the independent MUNICS (Drory et al. 2004) and COMBO-17 (Borch et al. 2006) fields. There are a few possibilities, beyond cosmic variance, which can explain this result. Although we conclude that the following are not the causes of the excess, we investigate them to show they are unlikely playing a role. The first is that the co-moving volumes we utilise to compute densities depends strongly on cosmological parameters. The first is that if we use a cosmology without a cosmological constant, an open universe

with $\Omega_m = 0.3$, the density contrast becomes larger. In fact, only values higher than $\Omega_\Lambda = 0.7$ helps alleviate the problem, but no reasonable values totally erase the excess.

Another issue we examined is whether the measurements of stellar masses are incorrect due to using the Bruzual & Charlot models to compute our mass to light ratios. Models, such as Maraston (2005) who include a newer treatment of thermally pulsing asymptotic giant branch (TP-AGB) stars in their models, can lower computed mass to light ratios for certain populations (see §3.3). As the TP-AGB stars have their most effect at an age of 1-2 Gyr, we investigate the fitted ages of our stellar populations to see if they are near these values. The average fitted ages for galaxies at $z > 0.6$ is roughly 4 Gyr for systems with $M_* > 10^{11} M_\odot$, and thus it is not likely that the exclusion of TP-AGB stars is influencing our mass measurements. However, fitted ages using TP-AGB stars might be lower, and in this case, it still remains possible that our masses are slightly overestimated. However, this likely cannot account for the entire increase, as the improved inclusion of the TP-AGB stars would lower the stellar masses by only 20% (§3.3). The real cause of the increase at $z \sim 0.9$ is likely cosmic variance, and even surveys larger than ours will be needed to probe the very massive end of the mass function with higher certainty.

4.3 Structures and Morphologies

Investigating the structures and morphologies of galaxies is becoming recognised as one of the most important methods for understanding galaxies (e.g., Conselice 2003; Trujillo et al. 2004; Cassata et al. 2005; Lotz et al. 2006). Since the morphologies and structures of galaxies have a direct relationship to their formation modes (i.e., disks, merging systems, etc), we study the morphological properties of our sample in some detail. The overlap of our NIR imaging and the ACS imaging in the EGS contains 506 galaxies with stellar masses $M_* > 10^{11} M_\odot$ at $z < 1.4$. For nearly all of these systems, their magnitudes are bright enough such that effects due to redshifts will not affect our ability to classify these systems either by eye, or through quantitative methods (e.g., Conselice et al. 2000c; Windhorst et al. 2002; Papovich et al. 2003, 2005; Taylor-Mager et al. 2006). Note that the following morphological and structural analyses are only within the ACS coverage of the EGS field.

4.3.1 Visual/Classical Morphologies

We study the structures and morphologies of our sample within the EGS using two different methods. The first is a simple visual estimate of morphologies based on the appearance of our galaxies in the ACS imaging. While the ACS imaging of the EGS field includes both F606W and F814W imaging, we only use the F814W band imaging in our structural/morphological analyses. The outline of our classification process is given in Conselice et al. (2005a). Basically, we place each galaxy into one of nine categories: compact, elliptical, lenticular (S0), early-type disk, late-type disk, edge-on disk, irregular, merger/peculiar, and unknown/too-faint. While classifying these galaxies by eye it became apparent that many of the early-types appear to have a slight distortion. We therefore added a sub-class of distorted ellipticals

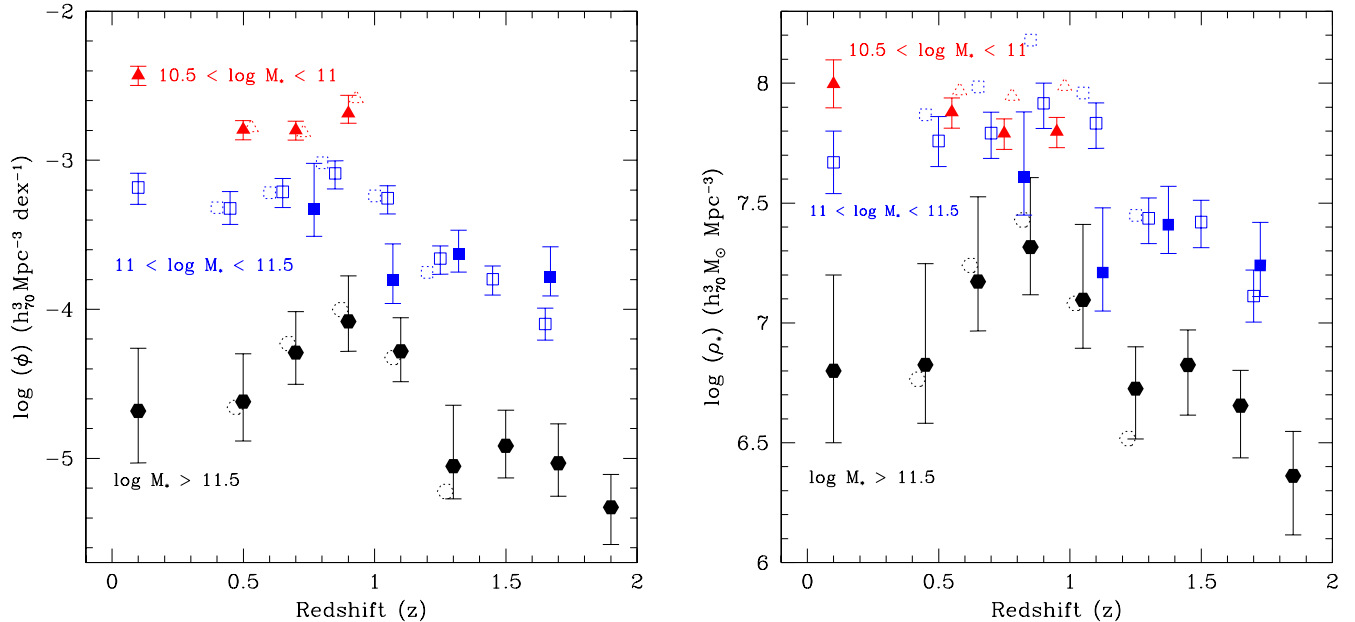


Figure 4. Left panel: the evolution in the number densities for galaxies of various masses between $z \sim 0.4 - 2$ with the spectroscopic and photometric redshift samples combined. Right panel: the stellar mass density evolution as a function of galaxy mass at the same redshift intervals. The points at $z \sim 0$ are taken from Cole et al. (2001), where the $z \sim 0$ point for the $M_* > 10^{11.5} M_\odot$ galaxies are corrected for the poor fit to these galaxies given in Cole et al. (2001) (see text). The error bars listed on both the numbers and mass densities reflect uncertainties from stellar mass errors, as well as cosmic variance, and counting statistics. The dashed symbols near each data point show how these values would change if just using photometric redshifts. The over-density at $z \sim 0.9$ remains even when we consider just the photometric redshifts. For comparison we show the mass densities for systems with $10^{11} M_\odot < M_* < 10^{11.5} M_\odot$ from Glazebrook et al. (2004) plotted as solid blue boxes. Note that shifts of ± 0.05 in redshifts have been applied so that data points and errors do not overlap.

to our classifications. These classifications are very simple, and are only based on appearance. No other information, such as colour or redshift, was used to determine these types. A short explanation of these types is provided below, with the number we find in each class listed at the end of each description.

(i) Ellipticals (E): Ellipticals are centrally concentrated galaxies with no evidence for lower surface brightness, outer structures. (263 systems, 68 of which are classified as disturbed Es)

(ii) Lenticular (S0): A galaxy is classified as an S0 if it appears elliptical-like, but contained a disk-like outer structure with no evidence for spiral arms, or clumpy star forming knots, or other asymmetries. (23 systems)

(iii) Compact - A galaxy is classified as compact if its structure is resolved, but still appears compact without any substructure. It is similar to the elliptical classification in that a system must be very smooth and symmetric. A compact galaxy differs from an elliptical in that it contains no obvious features such as an extended light distribution or envelope. (65 systems)

(iv) Early-type disks: If a galaxy contains a central concentration with some evidence for lower surface brightness outer light in the form of spiral arms or a disk, it is classified as an early-type disk. (28 systems)

(v) Late-type disks: Late-type disks are galaxies that appear to have more outer low surface brightness disk light than inner concentrated light. (18 systems)

(vi) Edge-on disks: disk systems seen edge-on and whose

face-on morphology cannot be determined, but is presumably an S0 or spiral. (12 systems)

(vii) Irregulars: Irregulars are galaxies that appear to have no central light concentration, and a diffuse structure, sometimes with clumpy material present. (2 systems)

(viii) Peculiars: Peculiars are systems that appear to be disturbed, or peculiar looking, including elongated/tailed sources. These galaxies are possibly in some phase of a merger (Conselice et al. 2003a), and are more common at high redshifts. (92 systems)

(ix) Unknown/too-faint: If a galaxy is too faint for any reliable classification it was placed in this category. Often these galaxies appear as smudges without any structure. These could be disks or ellipticals, but their extreme faintness precludes a reliable classification. (3 systems)

We repeat our visual classifications for a fraction of our sample, finding an initial misclassification at the 5% level. We also compared our eye-ball estimates to the CAS quantitative values discussed in §4.3.4, which allowed us to identify a significant fraction of the misclassified systems (see Appendix A), which were then corrected to their proper morphological type. We only perform these classifications out to $z \sim 1.4$ (cf. higher redshifts in Conselice et al. 2007a), and only use the F814W band for the classifications. This presents a potential k-correction issue, as the F814W band reveals bluer light at higher redshifts. However, through tests with the F606W band at redshifts where F814W probes well into the rest-frame optical, as well as tests on classifications in the HDF and Hubble Ultra Deep Field, show that

morphological typing within the F814W band gives very similar results, with at most a 5% difference between rest-frame B-band and the observed I-band at $z < 1.4$ (Conselice et al. 2005a).

When we discuss classifications in terms of early/mid/late types, these refer to: early (E/Compact/S0), mid (Sa-Sb), late (Sc-Irr). For the most part we find from our visual analysis that most of the $z < 1.4$, and $M_* > 10^{11} M_\odot$ systems, in which we can see structure, have an early-type morphology. There is however a small, but significant, morphological diversity among the $M_* > 10^{11} M_\odot$ galaxies. We find that over all redshifts, 69% of the $M_* > 10^{11} M_\odot$ systems are early-types (elliptical, S0, compact), while 10% are disks, and 18% are peculiars. This is perhaps a surprisingly high fraction of peculiars within our sample, and suggests that some of these systems are still undergoing some type of mass assembly, possibly through merging or star formation. This however changes when we examine only the most massive systems with $M_* > 10^{11.5} M_\odot$. These galaxies are $\sim 80 - 90\%$ early-type over all redshifts, with a roughly similar number of mergers and disks making up the remainder. These results remain essentially the same to within 5%, if we consider the Eddington bias bringing lower mass galaxies into our mass cuts due to observational uncertainty. This confirms and expands with a larger sample, earlier work on massive galaxies which also concluded that more massive galaxies appear to develop an early-type morphology before lower mass systems (Brinchmann & Ellis 2000; Bundy et al. 2005).

In Figure 5 we plot the visual estimates for how the morphological break-down for both the $M_* > 10^{11.5} M_\odot$ and $10^{11} M_\odot < M_* < 10^{11.5} M_\odot$ galaxies evolves from $z \sim 1.4$ to 0.1. The $z \sim 0$ points are based on morphologies from the RC3 catalogue, as described in Conselice (2006a). The most remarkable aspect of this evolution is that the fraction of elliptical galaxies with masses greater than $M_* = 10^{11} M_\odot$ is relatively constant out to $z \sim 1.4$, at about 70%. There is perhaps a slight increase for the $10^{11} M_\odot < M_* < 10^{11.5} M_\odot$ systems at $z = 1 - 1.5$, as seen in previous work (Bundy et al. 2005). Remarkably, there seems to be a gradual trend for the remaining 30% to transition from mergers/peculiars into disks. It is interesting that such massive disk galaxies exist at these redshifts, which must have evolved into the $M_* > 10^{11} M_\odot$ bin through star formation, or through a morphological transformation from an early-type to a spiral (§4.3.2).

In summary, what we find is that the majority of massive galaxies up to $z \sim 1.4$ have an early-type morphology (see also Bundy et al. 2005). This is consistent with the findings that most of these systems are already formed in terms of their stellar masses at similar epochs (§4.2). However, it is clear that $\sim 30\%$ of galaxies with $M_* > 10^{11} M_\odot$ are not early-types, which suggests that there is evolution in the massive galaxy population that cannot be seen simply through the evolution in number and mass densities. The disk galaxies we see suggest that there is some star formation occurring, and the peculiars suggest that there is merger activity. We investigate both of these galaxy-types, and what they imply for the evolution of the most massive galaxies, in the next sections.

4.3.2 Massive Disk Galaxies

As can be seen from Figure 5, there is a significant, $> 4\sigma$, increase in the number, and relative fraction, of massive $M_* > 10^{11} M_\odot$ disk galaxies at $z < 1.4$. This result is robust to morphological k-corrections (§4.3.1; Conselice et al. 2005), and shows a real increase in massive disk galaxies through time. We investigate the possible reasons for this increase in this section.

As already noted, there is a gradual transition for the non-ellipticals with $M_* > 10^{11} M_\odot$ to appear as peculiars at $z > 1$, and as disks at $z < 1$. What is likely occurring is that the higher redshift peculiars are transforming into ellipticals after they dynamically relax. This leaves the problem of why are there are significantly more disks at lower redshifts, and why the fraction of early-types does not change with redshift. That is, if the highest redshift peculiars are becoming ellipticals, we would expect the early-type fraction to increase at lower redshift, but it remains roughly constant. One possible scenario is that some of the already massive ellipticals acquire a disk through accretion of intergalactic gas, and the accretion of low-mass satellite galaxies (e.g., Abadi et al. 2003). Although candidates for this disk formation are seen at slightly higher redshifts both morphologically and through kinematics (e.g., Erb et al. 2003; Conselice et al. 2004; Labbe et al. 2004; Elmegreen et al. 2005; Forster-Schreiber et al. 2006; Genzel et al. 2006; Bouche et al. 2007), it is unlikely that these large disks without massive bulges are formed in this manner.

The rise of these massive disks are explainable by systems with disks masses $M_* < 10^{11} M_\odot$ at $z > 1$ being brought up into the $M_* > 10^{11} M_\odot$ bin through star formation or minor mergers. As we have seen earlier, the number densities of galaxies with $M_* > 10^{11} M_\odot$ increases slightly with time. Therefore these disk galaxies were likely lower mass ($M_* < 10^{11} M_\odot$) systems, and achieved $M_* > 10^{11} M_\odot$ status by $z \sim 0.5$ through star formation or minor merger accretion activity (§5.1). For structural reasons this seems like the most likely scenario, and can explain the nearly constant elliptical fraction, despite the morphological transformation of peculiars, by simply increasing the total number of $> 10^{11} M_\odot$ galaxies by adding new spirals.

This idea is backed up by the evolution in the number densities, and relative number fractions, of the different morphological types shown in Figure 5. The total number densities of disk galaxies at $z < 1$ is higher than the number densities of peculiar galaxies at $z > 1$. This means that it is difficult for the peculiars, without significant new star formation, to produce all of the spirals seen at lower redshifts. At the same time the peculiars are decreasing in number density at $1 < z < 1.4$, the densities of the ellipticals are increasing. This causal relationship is highly suggestive that these peculiars are transforming morphologically into early types by $z \sim 1$. After $z \sim 1$ there are very few peculiars in the mass range $10^{11} M_\odot < M_* < 10^{11.5} M_\odot$, and no further growth in the number densities of early types.

Another argument against a direct peculiar to spiral transition is the structures of these massive disks. The nine most massive spirals/disks in our sample are shown in Figure 6. As can be seen, these systems are often dominated by disk light, and do not appear to have particularly large bulges. Some systems also appear to have rings and bars. Be-

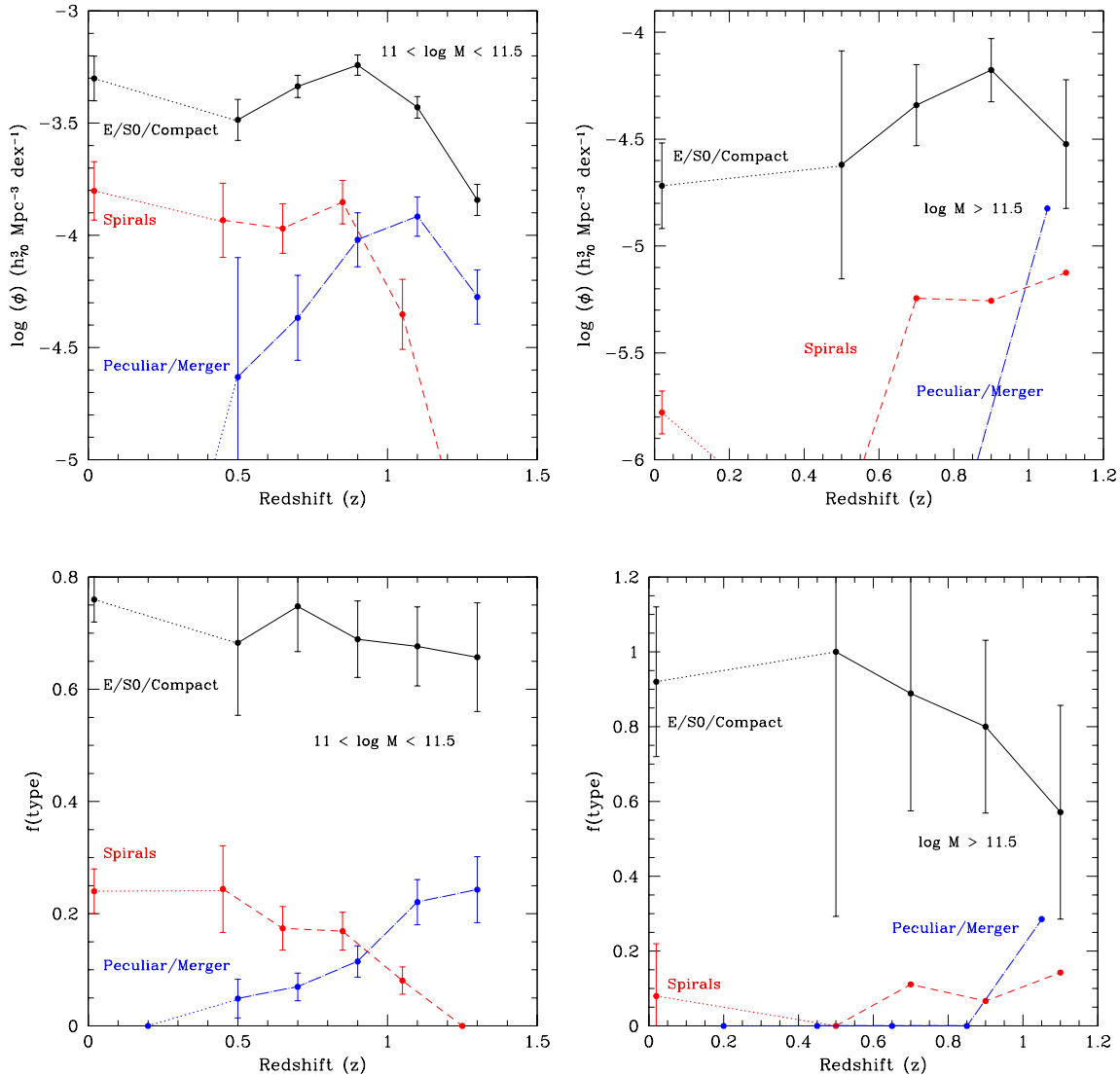


Figure 5. Visual estimates of the morphological evolution for the most massive galaxies within the EGS portion of our survey, where we have ACS data from Hubble. This figure is divided into two mass ranges and shows in the upper panels the evolution of galaxy number densities at $z < 1.4$, while the bottom panel shows the evolution in the relative numbers of different morphological types selected by mass. The left panels shows the morphological break down up to $z \sim 1.4$ for systems with $10^{11} M_{\odot} < M_{*} < 10^{11.5} M_{\odot}$. The right hand side shows the corresponding evolution for galaxies with $M_{*} > 10^{11.5} M_{\odot}$. The error bars on the $M_{*} > 10^{11.5} M_{\odot}$ galaxies are significantly higher than for the $10^{11} M_{\odot} < M_{*} < 10^{11.5} M_{\odot}$ galaxies due to the smaller number of galaxies, and are only plotted for the elliptical/S0s, although the peculiars/mergers and spirals have similar errors. Both plots demonstrate that ellipticals dominate the population up to $z \sim 1.4$. Interestingly, it also appears that the fraction of spirals increases from high to low redshift, while peculiars decline from higher to lower redshifts. The morphological fractions and densities form the $z = 0$ systems are taken from Conselice (2006a).

cause these spirals have such large disks and small bulges, it is unlikely that the peculiar galaxies at $z \sim 1.3$ are transforming into these systems. If this were the case, we would expect the spirals to show more disturbances, or at least a large bulge formed through the merger. Massive disk galaxies in previous work are also found to be largely in place in

terms of sizes, morphologies, and masses by $z \sim 1$ (Ravindranath et al. 2004; Jogee et al. 2004; Conselice et al. 2005b), thus any evolution in disks must be gradual. An interesting future study would be to study in detail these high mass disk galaxies at $z < 0.5$ to decipher their origin in more detail.

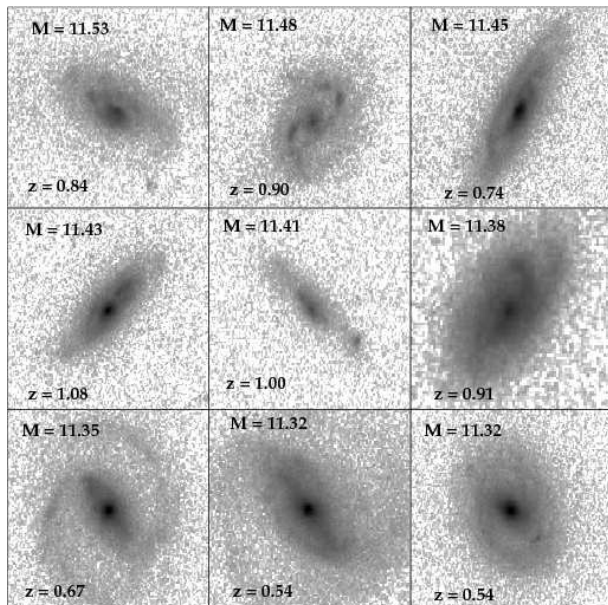


Figure 6. The most massive disk galaxies in our sample with the value of their stellar mass (in log M units), and their redshifts labelled. These disks have few tidal distortions due to interactions or minor mergers, and they all appear to lack large bulges. They also appear largely devoid of star formation, and occasionally they have rings and bars.

4.3.3 Disturbed Ellipticals

It is important to note that although early-types (classified E/S0/compact) dominate the galaxy population at both the $M_* > 10^{11} M_\odot$ and $M_* > 10^{11.5} M_\odot$ mass selection limits, these galaxies often contain evidence for morphological peculiarities. Usually these are in the form of outer low surface brightness features, or multiple cores. These are most likely the result of recent past merger activity in these galaxies, either through major or minor mergers. Examples of these distributed ellipticals are shown in Figure 7.

A total of 68 out of 263 ($26 \pm 3\%$) of the ellipticals with $M_* > 10^{11} M_\odot$ show some internal substructure visible by eye (Figure 7). As Figure 8 shows, the fraction of ellipticals with these distorted structures is relatively constant over time. There is perhaps a slight increase in this fraction at lower redshifts, which if real can be accounted for by surface brightness dimming. Peculiar ellipticals have been seen in other ways previously, such as through colour gradients and colour structures in ellipticals (e.g., Menanteau et al. 2005; Stanford et al. 2004; Teplitz et al. 2006), resulting from star formation and which may be related to the features seen here. These previous studies have generally found that the lower mass ellipticals contain these star formation signatures. These morphological disturbances however do not appear more common in the lower mass ellipticals, and in fact, 36% of the $M_* > 10^{11.5} M_\odot$ ellipticals show this signature - a higher fraction than for the $10^{11} M_\odot < M_* < 10^{11.5} M_\odot$ population. If these features are formed from a merger

of various types, then it would be an anti-downsizing signature, suggesting that many giant ellipticals are still forming at $z < 1.4$, perhaps through dry-merging.

4.3.4 CAS Structural Analysis

We use the CAS (concentration, asymmetry, clumpiness) parameters to probe the structures of our galaxies quantitatively. The CAS parameters are a non-parametric method for measuring the structures of galaxies on resolved CCD images (e.g., Conselice et al. 2000a; Bershady et al. 2000; Conselice et al. 2002; Conselice 2003). Our main purpose in using the CAS system is to identify relaxed massive ellipticals, as well as any galaxies that are involved in recent merger activity. The basic idea is that galaxies have light distributions that reveal their past and present formation modes (Conselice 2003). Furthermore, well-known galaxy types in the nearby universe fall in well defined regions of the CAS parameter space. We can then automatically determine the structures of galaxies and classify them according to where they fall in this space (Conselice 2003). For example, the selection $A > 0.35$ locates systems which are nearly all major galaxy mergers (Conselice et al. 2000b; Conselice 2003; Hernandez-Toledo et al. 2006; Conselice 2006b); although ‘dry’ mergers will not be detected easily through this method (Hernandez-Toledo et al. 2006).

We apply a revised CAS system to our massive galaxy sample to determine their structural parameters. There are two caveats to using the HST one orbit ACS imaging of these galaxies. The first is that there are morphological k-correction and surface brightness dimming effects which will change the measured parameters, such that the asymmetry and clumpiness indices will decrease (Conselice et al. 2000; Conselice 2003), and the concentration index will be less reliable (Conselice 2003). There is also the issue that systems at $z > 1.2$ are viewed in their rest-frame ultraviolet using ACS data, which means that there are complications when comparing their measured structures with the calibrated rest-frame optical indices for nearby galaxies.

Figure 9 shows the concentration/asymmetry and asymmetry/clumpiness projections of the CAS plane. As can be seen in the CA plane, the early-type galaxies mostly fall into the $z \sim 0$ calibrated early or mid-type region, and disks are found in the mid-type and late-type regions. Interestingly, the distorted (as selected by-eye) ellipticals are significantly more asymmetric than the normal ellipticals.

The CAS approach for classifying these galaxies is roughly similar to what the visual morphologies suggest, although there are important exceptions. Details of the differences between these two methods are further elaborated on in Appendix A. For the most part, galaxy types, as determined by eye, are where they are expected to be found on this diagram. One important exception is that many of the visually classified non-distorted early-types are not located in the corresponding $z \sim 0$ part of the CAS diagrams. While these systems have concentration indices similar to nearby giant ellipticals (Conselice 2003), they often have higher than expected asymmetry indices. An examination of these galaxies, and the residuals from a rotation and subtraction reveals that many of these systems have internal structures, likely resulting from mergers of various forms, that cannot be easily seen by eye.

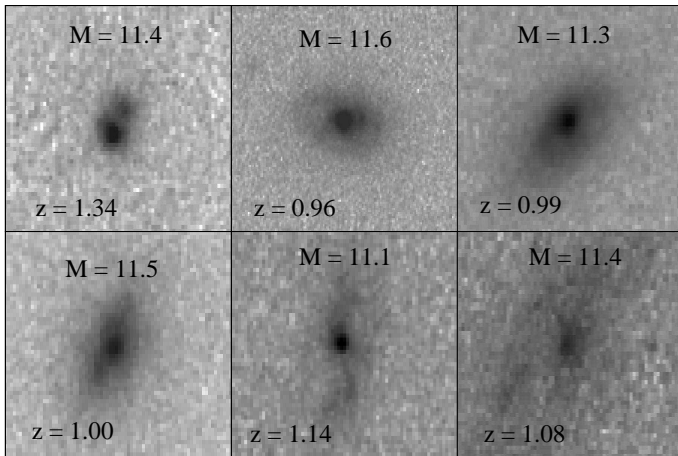


Figure 7. Images of six galaxies classified as distorted ellipticals. These are among the most peculiar of our sample, with most peculiarities not easily reproduced on paper, but easily seen with a viewer, and within the quantitative CAS parameters. Listed on each panel is the value of $\log M$ for each galaxy, as well as their redshift.

Furthermore, the SA plane (Figure 9) shows an interesting pattern, such that most of our galaxies appear to deviate from the $z \sim 0$ relation, shown by the solid line. This deviation is such that all galaxies are more asymmetric than their $z \sim 0$ counterparts, although the slope of the relationship between asymmetry and clumpiness is similar to that found at $z \sim 0$. This implies that galaxies of a given morphological type, particularly the early-types, have a higher degree of bulk asymmetry in their structures. The concentration and clumpiness values, which trace to first order the stellar mass and star formation, remain similar to what we expect from samples in the nearby universe. Finally, it appears that the most asymmetric systems, and those that deviate the most from the A-S relationship are the peculiar/merging systems, or those ellipticals that show some evidence for structure due to recent tidal events. This shows that our visual estimates of merging systems is borne out by this quantitative analysis.

4.3.5 Merger Fractions from CAS parameters

One of the great benefits of using the CAS system for finding mergers is that it allows us to quantify the merger fraction and merger rate, and the number of mergers occurring in a galaxy population (Conselice et al. 2003a; Conselice 2006).

The first observation we can derive from our CAS values is the evolution of the merger fraction. We determine the merger fraction for the $M_* > 10^{11} M_\odot$ galaxies using the criteria, outlined in Conselice (2006) of,

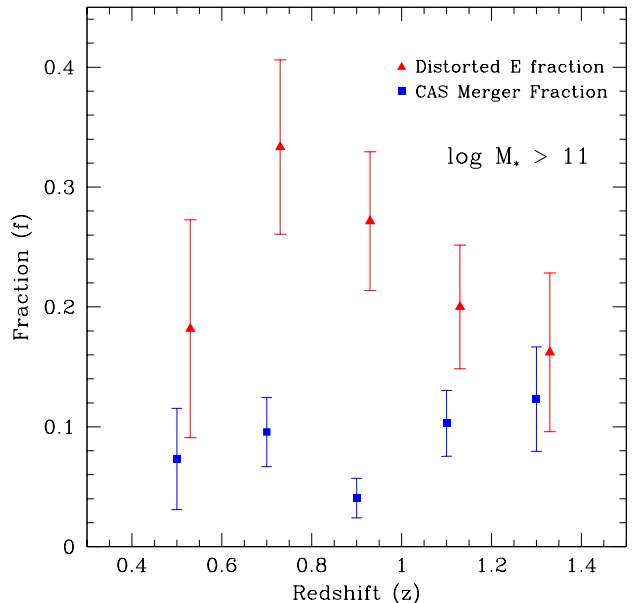


Figure 8. The evolution from $z \sim 1.4$ to 0.4 of the merger fraction derived through the CAS approach for galaxies with $M_* > 10^{11} M_\odot$. We find that the merger fraction as derived with the CAS parameters declines as $(1+z)^{1.3}$. Also plotted is the fraction of early types which are distorted within the same mass range of $M_* > 10^{11} M_\odot$. Note that like all of the structural and morphological plots, these data are only taken from the EGS.

$$A > 0.35, A > S. \quad (1)$$

Using these criteria, we determine the merger fraction for the $M_* > 10^{11} M_\odot$ galaxies in our sample (Figure 8). As can be seen, there is a slight increase with redshift in the merger fraction such that it increases as $(1+z)^{1.3}$, similar to the evolution seen in lower mass galaxies (Conselice et al. 2003; Bridge et al. 2007) up to $z \sim 1$.

By using the number densities for our systems, and the merger time-scales for our CAS method, we can calculate the merger rate for our $M_* > 10^{11} M_\odot$ galaxy sample. The number densities for our systems are taken directly from Table 2 in this paper, and the time-scales for merging are derived from equation 10 in Conselice (2006), based on N-body models analysed using the CAS approach. From this, we derive a merger CAS time-scale of $\tau = 0.43 \pm 0.05$ Gyrs for a galaxy with a mass of $3 \times 10^{11} M_\odot$. Note that this time-scale is not the total merger time, but the time-scale in which the CAS system would identify an ongoing merger. Details for how this time-scale is computed are included in Conselice (2006).

The merger rate for our systems can be calculated through the merger rate equation,

$$\mathcal{R}(z) = f_m(z) \cdot \tau_m^{-1} n_m(z) \quad (2)$$

where n_m is the number densities of objects, and f_m is the merger fraction. Note that this is not the galaxy merger fraction, which is the fraction of galaxies merging, which is roughly double the merger fraction (Conselice 2006). We find that statistically the merger rate for these $M_* > 10^{11}$

M_{\odot} galaxies is constant from $z \sim 0.4 - 1.4$, and is on average $\log \langle \mathfrak{R}(\text{Gyr}^{-1} \text{Gpc}^{-3}) \rangle = 4.3_{-0.7}^{+0.4}$.

We can furthermore calculate the total number of major mergers a galaxy with a stellar mass $M_* > 10^{11} M_{\odot}$ undergoes from $z \sim 1.4$ to $z \sim 0.4$ using equation (11) in Conselice (2006). We calculate that the average number of mergers a massive galaxy with $M_* > 10^{11} M_{\odot}$ will undergo from $z \sim 1.4$ to 0.4 is $N_m = 0.9_{-0.5}^{+0.7}$. Thus, on average a massive galaxy will undergo about one major merger from $z \sim 1.4$ to 0.4 , roughly consistent with previous results (Conselice 2006; Bell et al. 2006).

4.4 Star Forming Properties of Massive Galaxies

4.4.1 General Trends on the Colour-Magnitude Diagram

A major question concerning high-mass galaxies is whether or not these systems have ongoing star formation at high redshifts. While it is commonly thought that massive galaxies have finished their assembly and star formation by $z \sim 1$, our results suggest otherwise. This is not the first claim for this, as evidence has accumulated during the last few years that ellipticals, including massive ellipticals, tend to have some ongoing star formation at $z \sim 1$ (e.g., Stanford et al. 2004; Teplitz et al. 2006) and even at $z \sim 0$ (e.g., Donas et al. 2006). Star formation, as measured through blue colours, found in morphologically selected early-types, tends to be found in lower mass systems (Bundy et al. 2005). We therefore investigate the fraction of massive galaxies undergoing star formation during this time, and the amount of stellar mass added due to this star formation.

We begin our examination of the star forming properties of $M_* > 10^{11} M_{\odot}$ galaxies by examining their location on the rest-frame B-band absolute magnitude (M_B) vs. rest-frame colour ($(U - B)_0$) diagram (Figure 10). These quantities are inferred from the observed magnitudes through model fitting, utilising the redshift and a series of k-corrections (Willmer et al. 2006). Galaxies appear to separate into a red-sequence and a blue cloud in this parameter space (e.g., Strateva et al. 2001; Im et al. 2002; Baldry et al. 2004; Bell et al. 2004; Faber et al. 2005). The evolution of galaxies on the colour-magnitude diagram has potential meaning for understanding how galaxy evolution occurs. In Figure 10 we plot the $(U - B)_0$ vs. M_B diagram for galaxies in our fields, with the most massive galaxies with $M_* > 10^{11.5} M_{\odot}$ and $10^{11} M_{\odot} < M_* < 10^{11.5} M_{\odot}$ labelled. The dividing line between red-sequence and blue cloud galaxies is shown as the dotted line in Figure 10, taken from Faber et al. (2005);

$$(U - B)_0 = -0.032 \times (M_B + 21.52) + 0.454 - 0.25. \quad (3)$$

We find at the highest redshift bin, $1.2 < z < 1.4$, a significant number of massive galaxies that are not on the red-sequence. In general, the number of massive galaxies on the red-sequence increases at lower redshifts. This is also true when we plot these galaxies in terms of their morphologies, where we find that many early-type galaxies are not on the red-sequence.

The quantification of the fractional evolution of galaxies on the red-sequence is displayed in Figure 11. This shows that the most massive systems with $M_* > 10^{11.5} M_{\odot}$ generally fall in the red-sequence region at all redshifts, but with a significant number of systems in the blue cloud region at

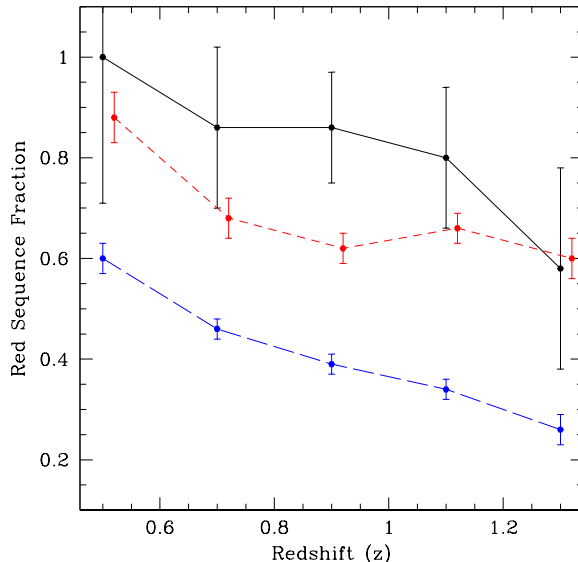


Figure 11. The fraction of galaxies of various masses which are on the red-sequence as defined in §4.4.1. The solid upper line shows the evolution of the fraction of galaxies with $M_* > 10^{11.5} M_{\odot}$ which are on the red-sequence, while the red short-dashed and blue long-dashed lines show the evolution for systems with $10^{11} < M_* < 10^{11.5} M_{\odot}$, and $10^{10.5} M_{\odot} < M_* < 10^{11} M_{\odot}$.

$z > 0.8$. As Figures 10 and 11 demonstrate, the fraction of galaxies on the red-sequence, with colours redder than the value given in eq. (3), increases with time at all masses. At the highest redshifts we can probe star formation, at $z \sim 1.3$, about 60% of the $M_* > 10^{11.5} M_{\odot}$ galaxies are on the red-sequence, yet this fraction increases to $100_{-26}^{+0} \%$ by $z \sim 0.4$. Galaxies with lower masses show a similar pattern, yet lower mass galaxies always have a lower fraction of galaxies on the red-sequence at all redshifts, up to $z \sim 1.4$.

This also leads to a very important conclusion regarding the red-sequence and high mass galaxies. Previous studies have examined the increase of the amount of stellar mass on the red-sequence, finding as much as a factor of two increase since $z \sim 1$ (Bell et al. 2004; Faber et al. 2005). However, this increase is due to galaxies appearing on the red-sequence, which were previously blue, and not due to in-situ growth on the red-sequence itself. This can be clearly seen in Figure 11 where the massive galaxies are gradually moving onto the red-sequence with time, which can also be seen in the decline in the number of blue massive galaxies found in the universe since $z \sim 1$. This is not consistent with the idea that the red-sequence grows solely through the so-called ‘dry mergers’. Although merging may be present within the red-sequence, and within our massive galaxy sample, it does not appear to be the dominate method whereby the red-sequence grows.

4.4.2 Quantification of Star Formation

We quantify the star formation in our sample of massive galaxies using [OII] line equivalent widths from DEEP2 spectroscopy, and through MIPS $24\mu\text{m}$ fluxes from Spitzer MIPS imaging. Over half of our total sample (spectroscopic

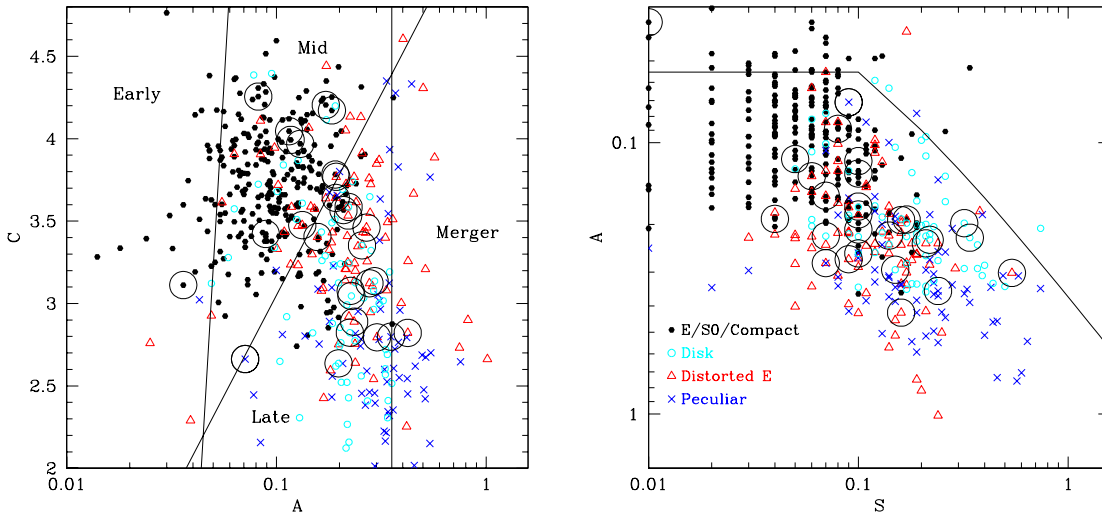


Figure 9. The concentration-asymmetry, and asymmetry-clumpiness projections of CAS space as occupied by galaxies with $M_* > 10^{11} M_\odot$. Points on this diagram are ellipticals/S0/compact (black solid circles), peculiar ellipticals (red triangles), peculiars/mergers (blue crosses), and disks (cyan open circles). Circled objects are those detected in the X-ray by Chandra. The lines denoting different galaxy types are from a $z \sim 0$ calibration described in Conselice (2003). The solid line in the A-S projection shows the relationship between these two parameters in the nearby universe for normal non-merging galaxies. Note that few of the visually classified normal ellipticals appear in the corresponding part of CAS parameter space due to their slightly high asymmetries. This can also be seen for all galaxies in the clumpiness-asymmetry diagram, showing that most of these asymmetries are produced by large-scale features, and not star formation.

and photometric redshift combined) do not have measured redshifts or [OII] emission line measurements. As such, we are forced to utilise the $24\mu\text{m}$ photometry to measure the star formation rate for the bulk of our systems. As we only have MIPS imaging in the EGS, we limit our analysis of star formation rates to galaxies in this field. Our star formation measures utilise the [OII] line, when available, added to the star formation measured from the $24\mu\text{m}$ fluxes. When [OII] is not available, the star formation rate is measured just using the MIPS fluxes.

To utilise the $24\mu\text{m}$ fluxes, we first convert the $24\mu\text{m}$ flux into a total IR luminosity $L(8 - 1000\mu\text{m})$ utilising templates from Dale & Helou (2002), as parameterised by LeFloc'h et al. (2005). We then calculate the obscured star formation rate in these systems through the equation,

$$\psi(\text{IR})(M_* \text{ yr}^{-1}) = 9.8 \times 10^{-11} \times L_{\text{IR}}, \quad (4)$$

which was derived in Bell et al. (2005). Equation (4) uses a Kroupa/Chabrier initial mass function, the same as we have used to calculate our stellar masses.

As is becoming clear, it is possible that both the [OII] and the MIPS fluxes could result from AGN emission. In the following analysis we have therefore removed galaxies which have been detected in X-rays, to avoid the most egregious cases of AGN contamination from our sample. Out of our sample of 1151 MIPS sources with $M_* > 10^{11} M_\odot$ at $0.4 < z < 1.4$, we find that 105 or $\sim 10\%$ are detected in X-rays. The X-ray properties of our sample are discussed in §4.5.

The star formation rate measured using the [OII] line is calculated through the equation,

$$\psi([\text{OII}])(M_* \text{ yr}^{-1}) = 10^{-11.6-0.4(M_B - M_{B\odot})} \times \text{EW}_{[\text{OII}]}, \quad (5)$$

where we are forced to use the equivalent width of the line instead of the flux, as the DEEP2 spectroscopy is not flux calibrated.

Although we do not include sources detected in X-rays in our star formation analysis, there is still some chance that the [OII] emission arises from AGN (Yan et al. 2006). This is mostly an issue for line emission from red galaxies, and usually these sources are LINERs. We cannot utilise line ratios to test this idea, as we do not have $\text{H}\alpha$ or [NII] equivalent widths. We can however examine the equivalent width ratios of the [OIII] and [OII] lines. We find that this ratio, $[\text{OIII}] \lambda 5007 / [\text{OII}] \lambda 3727$ is nearly always in the region of star forming galaxies within our sample. This is consistent with the idea that bluer galaxies, which dominate our sample at these higher redshifts, have line ratios consistent with star formation (Yan et al. 2006).

Perhaps surprisingly, about half of our massive galaxies are detected at $24\mu\text{m}$. After matching the MIPS and [OII] star formation indicators, we find that $\sim 40\%$ of the $M_* > 10^{11} M_\odot$ systems at $0.4 < z < 1.4$ are detected to our $24\mu\text{m}$ depth. A total of $37 \pm 5\%$ of the systems at $M_* > 10^{11.5} M_\odot$ are detected at $24\mu\text{m}$, with an average star formation rate of $70 M_\odot \text{ yr}^{-1}$. For systems within the mass range $10^{11} M_\odot < M_* < 10^{11.5} M_\odot$, we find a higher fraction of MIPS detected systems, with a fraction of $45 \pm 1\%$, at an average star formation rate of $\sim 40 M_\odot \text{ yr}^{-1}$.

When we compare star formation rates derived from the [OII] line with those from the $24\mu\text{m}$ flux, we find that the $24\mu\text{m}$ derived star formation rates are always much higher. Furthermore, we find little correlation between the two indicators. This is an indication that [OII] and IR star formation indicators are measuring two different aspects of the star formation in a galaxy, or that one, or both, of these methods is mis-measuring the star formation. A more detailed discussion of different star formation indicators using emission lines and MIPS fluxes is included in Weiner et al. (2006).

For galaxies with stellar masses $10^{11} M_\odot < M_* < 10^{11.5}$

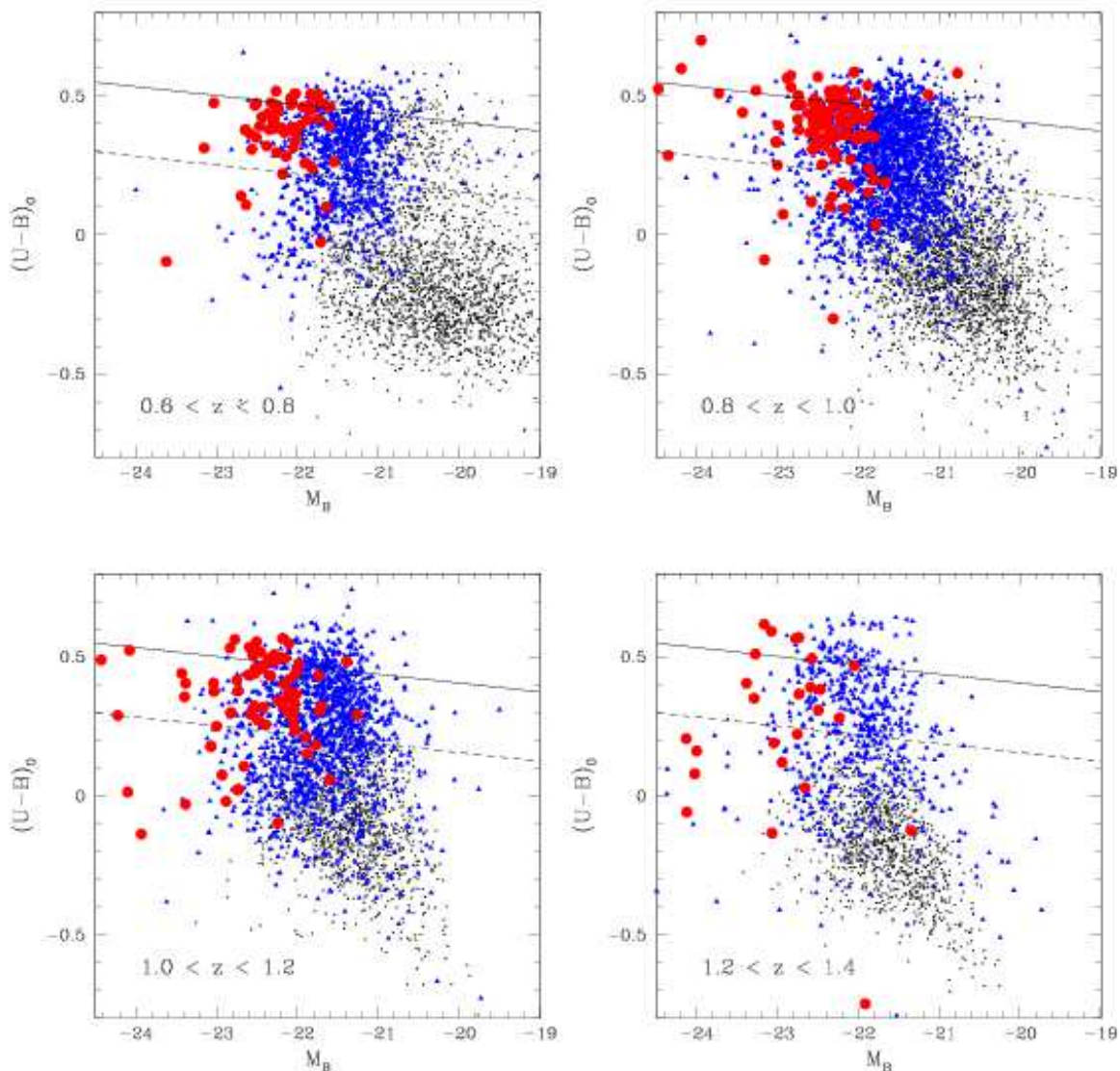


Figure 10. The $(U-B)_0$ vs. M_B diagram for galaxies with $M_* > 10^{10.5} M_\odot$ from $z = 0.6$ to $z = 1.4$. Included are both the spectroscopic and photometric redshift samples. The large red points on each panel are for those galaxies with $M_* > 10^{11.5} M_\odot$. The blue triangles show the location of the systems with $10^{11} M_\odot < M_* < 10^{11.5} M_\odot$. The solid line in each diagram shows the location of the red-sequence as defined in Faber et al. (2005), and the dashed line is the demarcation between red and blue galaxies.

M_\odot , we find that the fraction of galaxies undergoing star formation remains roughly similar at all redshifts. Circumstantially, this is consistent with the fact that the fraction of spirals+peculiar in this mass cut is roughly constant throughout this redshift range. Interestingly, the fraction of systems which are undergoing star formation is higher than the non-elliptical fraction, showing that some morphologically classified massive ellipticals must be undergoing star formation.

There is a slight decline with redshift in the fraction of $M_* > 10^{11.5} M_\odot$ galaxies with a significant $24\mu\text{m}$ detection. The fraction declines from 33% at $1.2 < z < 1.4$ to 14% at $0.4 < z < 0.6$, which is consistent with a drop in the morphological fraction of non-ellipticals. This is however certainly a lower limit to the evolution, as the number of galaxies we

can detect at $24\mu\text{m}$ declines at higher redshifts. The redshift distribution of star formation rate, as measured through the combined star formation seen in the infrared and [OII] line is shown in Figure 12, for systems with $M_* > 10^{11} M_\odot$.

As Figure 12 shows, we are incomplete in measuring the star formation rate at the highest redshifts of our sample. This is due to the MIPS imaging becoming incomplete at the highest redshifts. When we derive the total star formation history, we correct for this by assuming that the relative star formation rate distribution of our sample, that is the relative number of galaxies at a given star formation rate, is the same at all redshifts. This does not assume that the normalisation of the distribution is the same, simply that the shape of the star formation distribution function is similar at high and low redshift. This correction is however small,

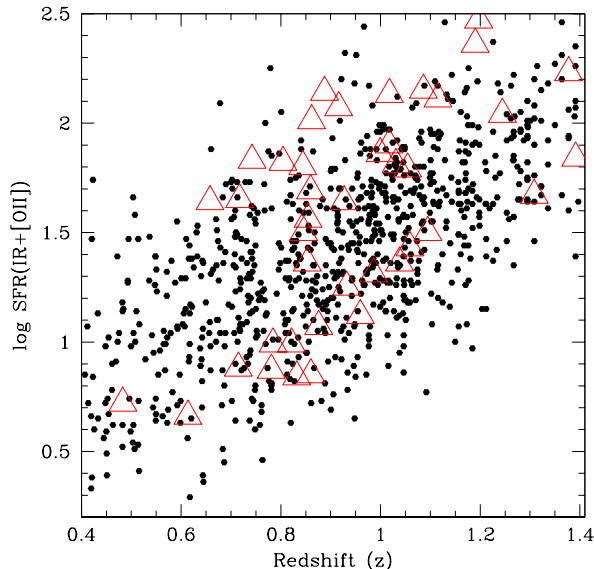


Figure 12. The total star formation rate, found by adding the MIPS infrared fluxes and [OII] line equivalent widths, as a function of redshift for our sample. The large open red triangles show the location of galaxies with $M_* > 10^{11.5} M_\odot$, while the solid dots show the location of galaxies with $10^{11} M_\odot < M_* < 10^{11.5} M_\odot$.

and only accounts for a 30-40% increase in the total star formation rate density.

We determine how the star formation rate has evolved within our sample by examining how the total integrated star formation density changes as a function of time and stellar mass (Figure 13). We find, similar to previous studies utilising IR star formation indicators (e.g., Le Floc’h et al. 2005), a decline at lower redshift for our sample, as seen in the entire field galaxy population (e.g., Lilly et al. 1995) out to $z \sim 1$. The less massive galaxies have a higher average star formation rate per unit time, and have a softer more gradual decline at lower redshift, compared with the $M_* > 10^{11.5} M_\odot$ galaxies.

When we fit these star formation histories up to their plateau (i.e., at $z \sim 1$) as a power law $\sim (1+z)^\alpha$ we find differences between our two mass ranges. For systems with $M_* > 10^{11.5} M_\odot$, we fit $\alpha = 6 \pm 2.2$, and for systems with $10^{11} M_\odot < M_* < 10^{11.5} M_\odot$ we fit $\alpha = 4.1 \pm 0.64$. The overall decline in the entire galaxy population’s star formation history can be parameterised as $\alpha = 3 - 4$ (Hopkins 2004; Le Floc’h et al. 2005). It appears that while the $10^{11} M_\odot < M_* < 10^{11.5} M_\odot$ galaxies have a similar decline as the overall field, the highest mass galaxies show a marginally faster decline.

4.4.3 Stellar Mass Growth from Star Formation

We can use our measured star formation rate densities to determine how much stellar mass is added to our massive galaxy sample through the star formation process. As we are averaging over the entire sample, we do not need to worry about the particular time-scales of the star forma-

tion induced in these systems, although the star formation time-scales are likely long (Noeske et al. 2007a,b). In these calculations we assume that the star formation rate density remains the same through a redshift bin. Thus, we can calculate the amount of new mass in stars created through the star formation process simply by integrating the star formation rate density throughout the redshift bin of interest. This calculation is independent of whether the star formation is produced in multiple short bursts, or in stochastic star formation occurring through time, as both scenarios give the same result.

Figure 14 shows the stellar mass evolution, and the amount of mass added to our sample due to star formation, as a function of redshift. This figure is constructed with the mass change referenced to the stellar mass density at $z \sim 1.3$, in each bin. The solid and short-dashed lines show the amount of stellar mass added due to star formation within the same bins, to galaxies with $10^{11} M_\odot < M_* < 10^{11.5} M_\odot$ and $M_* > 10^{11.5} M_\odot$, respectively, as a function of redshift.

While the stellar mass increase with time due to star formation matches within 1-3 sigma the amount of mass at redshifts $z < 1.3$ it is not clear that, when considered together, whether the star formation by itself can account for changes in the mass function with time. We examine this statistically by determining the probability that the stellar mass increase due to star formation can account for the mass changes seen at all redshifts. This test shows that the probability that star formation, within a bin, is alone responsible for the stellar mass increase is 0.13%, at 3σ , for the $10^{11} M_\odot < M_* < 10^{11.5} M_\odot$ systems, and 0.0025% (3.5σ) for the $M_* > 10^{11.5} M_\odot$ systems. Therefore, statistically star formation by itself, within a bin, cannot account for the observed mass changes at the highest redshift bins. We however do not consider here the effects of galaxy transfer between mass bins, although we do so in §5.1. Note that although statistically the changes in the mass function are not significant at $> 3\sigma$, there is a general trend such that the mass density increases, particularly at $z > 1$. Our goal here is to determine whether the stellar mass created from the star formation is consistent with the observed change.

The stellar mass added from star formation is therefore unlikely able to account for the changes in the stellar mass density seen as a function of stellar mass. This result is however dominated by the large error bars on the mass density. As the only other way to obtain stellar mass growth is through galaxies entering bins from lower masses and merging, we investigate these processes and derive statistically how much merging might be occurring from $z \sim 1.3$ to $z \sim 0.4$ in §5.1.

4.5 Active Galactic Nuclei

To determine the unobscured AGN properties of our massive galaxy sample we match our galaxies with a preliminary catalog of X-ray fluxes from Nandra et al. (2007, in preparation). The Nandra et al. (2007) study is a major Chandra program to cover an area of 0.6 deg^2 in the EGS with a depth per pointing of 200 ks in both the hard (3.1 \AA , 3 keV) and soft (12.4 \AA , 1 keV) bands. A basic description of this X-ray data is given in Nandra et al. (2007), Georgakakis et

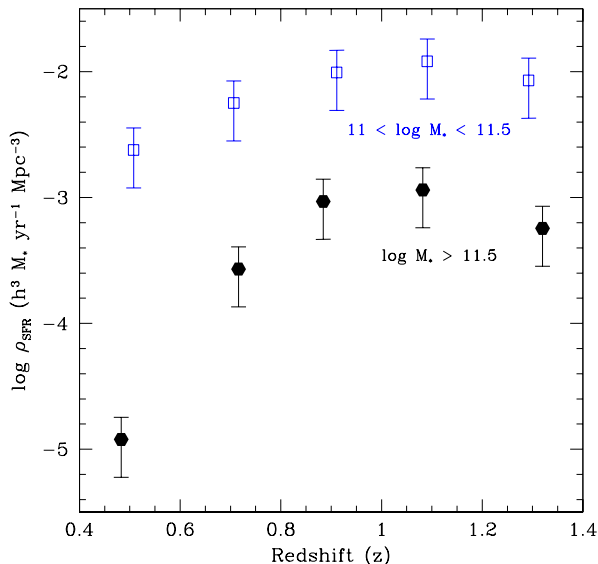


Figure 13. The star formation rate density (ρ_{SFR}) as a function of redshift up to $z \sim 1.4$. Plotted are the measured star formation rates for both the $10^{11} M_{\odot} < M_{*} < 10^{11.5} M_{\odot}$, and the $M_{*} > 10^{11.5} M_{\odot}$ samples.

al. (2007) and Davis et al. (2007), with a full description to appear in Nandra et al. (2007).

We matched our stellar mass selected catalog to this X-ray catalog, with a valid match occurring for those within $1-3''$. There are 123 galaxies in our sample of $M_{*} > 10^{11} M_{\odot}$ that have a matching X-ray detection down to a limit of $8.2 \times 10^{-16} \text{ erg s}^{-1}$ in the hard band, and $1.1 \times 10^{-16} \text{ erg s}^{-1}$ in the soft band. This accounts for a surprisingly high fraction (5%) of the entire $M_{*} > 10^{11} M_{\odot}$ sample. To these limits, there are also eight galaxies with $M_{*} > 10^{11.5} M_{\odot}$ with an X-ray detection. In both ranges these X-ray sources are found in roughly 5% of the sample.

The properties of X-ray sources in deep extragalactic near infrared and optical surveys have been discussed in several previous papers (e.g., Hornschemeier et al. 2003; Grogin et al. 2005; Lehmer et al. 2005; Georgakakis et al. 2006; Nandra et al. 2006). These previous studies have generally found that X-ray sources are in evolved, concentrated galaxies up to $z \sim 4$ (Grogin et al. 2005; Lehmer et al. 2005). This may imply that X-rays are tracing only one phase of the evolution of an active galaxy, yet for the purposes of this paper we examine these X-ray sources with the assumption that they probe a representative sample of galaxies with active galactic nuclei.

Since we are interested in the spectral properties and the luminosities of the AGN in our sample, we convert our measured X-ray fluxes from the Nandra et al. (2007) catalog into X-ray luminosities utilising the formula:

$$L_x = \text{flux}(2-10\text{keV}) \times 4\pi D_L^2 (1+z)^{\Gamma-2}, \quad (6)$$

where D_L is the luminosity distance and Γ is a quantification of the spectral shape. To obtain a flux which is independent of intrinsic absorption we calculate our luminosities using $\Gamma = 1.9$, the intrinsic spectral shape of an AGN, and always

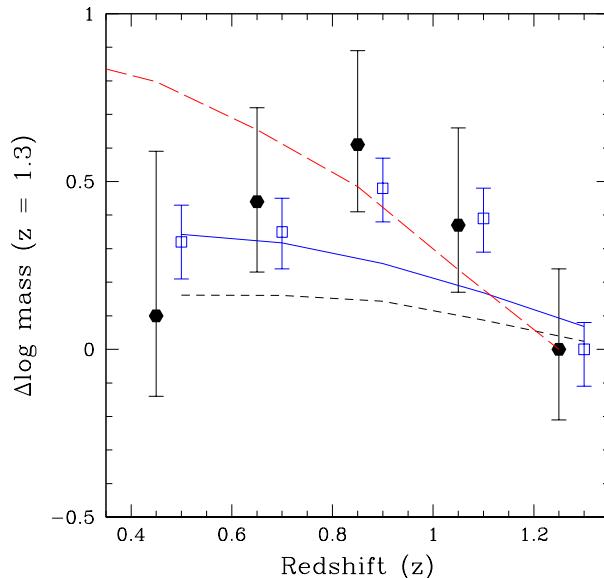


Figure 14. The evolution in the mass density as a function of redshift and stellar mass. The solid dots and open boxes represent the evolution of galaxies with stellar masses $M_{*} > 10^{11.5} M_{\odot}$ and $10^{11} M_{\odot} < M_{*} < 10^{11.5} M_{\odot}$, respectively, referenced to their stellar mass densities at $z \sim 1.3$. The solid blue line shows the evolution in the amount of stellar mass added from the $z \sim 1.3$ bin as a function of redshift from galaxies with stellar masses of $10^{11} M_{\odot} < M_{*} < 10^{11.5} M_{\odot}$. The short-dashed line shows a similar increase in stellar mass due to star formation for the $M_{*} > 10^{11.5} M_{\odot}$ systems. The long-dashed red line shows the relative increase in the stellar mass for the $M_{*} > 10^{11.5} M_{\odot}$ systems due to stellar mass brought up from the $10^{11} M_{\odot} < M_{*} < 10^{11.5} M_{\odot}$ bin due to star formation.

use the hard band flux (2-10 keV), as it is the least affected by absorption.

We also investigate the hardness ratios (HR),

$$\text{HR} = \frac{(\text{counts}_{\text{shard}} - \text{counts}_{\text{soft}})}{(\text{counts}_{\text{shard}} + \text{counts}_{\text{soft}})}$$

of our X-ray sources, finding a range of values, with an average hardness ratio of -0.05 ± 0.58 for the full sample at $M_{*} > 10^{11} M_{\odot}$. However, we find that the most massive systems with $M_{*} > 10^{11.5} M_{\odot}$ have an average hardness ratio of -0.50 ± 0.38 , showing that, on average, the most massive galaxies have soft spectra, likely from unobscured AGN. This may be a further sign of downsizing, where the AGN in the higher mass galaxies becomes less obscured due to the removal or dissipation of the obscuring mechanism earlier than in lower mass galaxies.

Figure 15 shows our basic X-ray analysis results in a graphical format, where the stellar masses of our galaxies with an X-ray detection in the EGS are plotted with their X-ray luminosities, as defined in equation (4). The morphological types and hardness ratios of these sources are also labelled. The X-ray sources are also circled on the CAS diagrams in Figure 9.

We generally find no correlation between X-ray source hardness ratio, X-ray luminosity or host galaxy stellar mass. However, our range in stellar mass is limited, and this should

not be interpreted as a complete study of AGN, but simply as a study of the X-ray sources associated with massive galaxies.

There is one interesting trend, which is that the X-ray sources in massive galaxies tend to be found in peculiars and distorted early-types. For the overlapping sample of 29 galaxies with $M_* > 10^{11} M_\odot$ that have both X-ray and HST imaging, we find that $\sim 45 \pm 12\%$ are either peculiar galaxies or distorted ellipticals. The remainder are $34 \pm 11\%$ normal elliptical/S0/compact and $21 \pm 8\%$ disks. This becomes even more significant when we determine what fraction of each morphological type is detected in the X-rays. When we do this comparison, we find that $\sim 15\%$ of the distorted ellipticals are X-ray detected, while only 3.5% of the E/S0/compact galaxies are detected.

This may appear to disagree with previous studies, such as Grogin et al. (2005) who found that X-ray sources are largely in low asymmetry and highly concentrated galaxies. We find that some of our X-ray sources have a large concentration index (Figure 9), and some of the peculiar ellipticals have a modest asymmetry, but they are not in the merger region at $A > 0.35$. It is likely that these earlier studies missed the fact that a significant fraction of the X-ray sources in the highest mass galaxies are found in early-type galaxies with peculiar structures. Since it is likely that these structures were produced in some type of a merger several Gyr earlier, we are potentially witnessing the remnant AGN activity produced in the last merger event. These earlier studies of AGN morphology also were not mass selected, as is our sample. It is furthermore possible that we are not able to detect the ongoing peculiar galaxies merging, in X-rays, due to deep obscuration, although this idea needs to be tested in more detail in a future study.

5 DISCUSSION

The last few years have seen a number of studies examine similar issues as this paper, with many studies concluding that massive galaxies, typically those with $M_* > 10^{11} M_\odot$, are largely formed by $z \sim 1$. This is statistically found to be the case in this paper, to within a factor of 2-3, in terms of measured mass and number densities, for systems with $M_* > 10^{11} M_\odot$ from $z \sim 1$, although there is some evolution from $z \sim 1.4$. A scenario where the number and mass densities of $M_* > 10^{11} M_\odot$ galaxies does not change at $z < 1.4$ can be ruled out at $> 8 \sigma$ confidence.

While we, and others, have found that the number and mass densities for massive galaxies are similar at $z < 1$, this does not necessarily imply that there is no evolution in this population. As we have discussed, there can be as much as a factor of three in evolution which we could not identify due to the uncertainties in the process of measuring stellar masses, and computing their number densities. It is likely that other methods besides densities, are need to conclusively argue whether massive galaxies are finished forming by $z \sim 1$. While we can rule out increases in densities that are a factor of three or greater, we cannot conclude that our that massive galaxies are not increasing in number and mass density by a factor of 2 or 3. The fact that we find a high fraction of massive galaxies that are forming stars (40%),

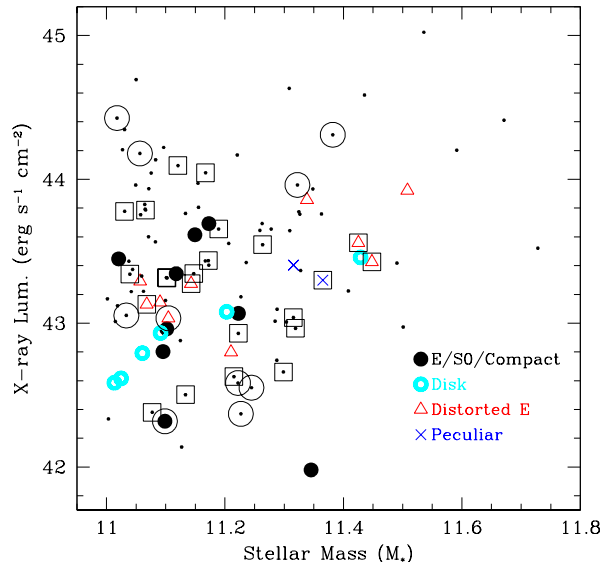


Figure 15. The relationship between the stellar masses of our X-ray detected massive galaxy sample and their X-ray luminosities as measured with Chandra. Sources with corresponding ACS imaging are labelled using the same scheme in Figure 9. Sources with soft hardness ratios < -0.5 are circled, while those with hard ratios > 0.5 are squared.

and which are non-elliptical (30%), at $z \sim 1$ alone suggests that there is some evolution.

One issue which is not clear is how much of the merger and star formation process, and especially the controversial and hard to find dry mergers, are responsible for the addition of mass in massive galaxies at these redshifts. We can address this using just our mass functions, and the measured star forming histories for galaxies with $M_* > 10^{11} M_\odot$, and $10^{11} M_\odot < M_* < 10^{11.5} M_\odot$. While the star formation history matches the observed increase in the stellar mass to within $< 3 \sigma$ at any one redshift, the fact that the star formation history is consistently lower at all redshifts implies that star formation, within a bin, cannot account for the total increase in stellar mass. This shows that part of the mass growth in these systems must be accounted for by mergers, or as we examine below, galaxies with masses lower than the $10^{11.5} M_\odot$ stellar mass limit evolving into the higher mass bin due to star formation and/or merging.

We find a higher probability that star formation can account for the increase in the mass density for systems with $10^{11} M_\odot < M_* < 10^{11.5} M_\odot$, with a 0.13% chance ($\sim 3 \sigma$). It appears however that for all galaxies with $M_* > 10^{11} M_\odot$, additional mass is added to these redshift bins over that which is seen in the star formation. Between the bins $M_* > 10^{11.5} M_\odot$ and $10^{11} M_\odot < M_* < 10^{11.5} M_\odot$ we can determine the mass transfer due to star formation. We calculate this in the next section after making a few assumptions concerning the distribution of galaxies within these bins, and how the star formation seen within these bins is distributed.

5.1 Evolution of Number Densities

In this section we examine ways in which galaxy mass functions can evolve due to star formation and merging. We consider star formation within a given mass bin, star formation at a lower mass bin, and mergers within a lower mass bin. Note that mergers within a given bin will never increase the total mass within that bin, unless star formation is triggered with the merger. It can however lower the number densities of galaxies within a bin.

Consider the change in the total stellar mass within a mass range of δM at a mass of M_0 . We can express the evolution of the mass function within δM between redshifts $\delta z = z_2 - z_1$ as,

$$\Delta M(M_0 + \delta M, \delta z) = \Sigma M_{\text{sf}} + \Sigma M_{\text{merg}}^{\uparrow} + \Sigma M_{\text{sf}}^{\uparrow}, \quad (7)$$

where ΔM is the change in the total amount of mass density within the mass bin between M_0 and $M_0 + \delta M$, and z_1 and z_2 . ΣM_{sf} is the amount of mass density within this bin added due to star formation within this mass bin, $\Sigma M_{\text{merg}}^{\uparrow}$ and $\Sigma M_{\text{sf}}^{\uparrow}$ are the amounts of stellar mass density added to the $M_0 + \delta M$ bin from mergers, and star formation which were initially in galaxies at $M_* < M_0$. Likewise, these terms should include mass density which has left the bin due to mergers and star formation. If we consider the $M_* > 10^{11.5} M_{\odot}$ bin, or any bin which is defined to be simply greater than a given mass, this additional term is zero.

These terms can be computed in the follow ways. For the star formation within the bin, where galaxies have an initial stellar mass between $M_0 < M_* < M_0 + \delta M$, we can write the mass added from star formation as,

$$\Sigma M_{\text{sf}} = \Sigma \psi_{\text{sf}} \cdot \tau(z_2 - z_1). \quad (8)$$

Where in equation (8), ψ_{sf} is the star formation rate density and τ is the time interval between redshifts z_1 and z_2 . This is the quantity plotted as the short-dashed and solid lines in Figure 14, and which falls short of accounting for the possible growth of stellar mass within these massive galaxies (§4.4.3).

Because the star formation within these bins cannot account for the change in the number and mass densities for massive galaxies (§4.4.3), the increase in stellar mass must be brought about from galaxies that were previously at lower masses. This increase must be produced by mass entering the bin through star formation or merging. Since star formation is in principle easy to directly study and trace, we will examine this aspect first.

To examine how much stellar mass is added to a bin of lower stellar mass, we must consider the star formation rate in galaxies in the lower mass bins. If the width of a lower stellar mass bin is δM_{lower} , then the amount of mass added per galaxy ($\delta M_{\text{sf,lower}}$) within a redshift and mass bin is given by

$$\delta M_{\text{sf,lower}} = \frac{\psi_{\text{sf,lower}} \cdot \tau(z_2 - z_1)}{\phi_{\text{lower}}}, \quad (9)$$

where ϕ_{lower} is the number density of galaxies in the lower mass bin. If we assume that galaxies are distributed evenly within their mass bin, δM_{lower} , then the fraction of galaxies within this bin which leave the bin due to star formation is simply $\delta M_{\text{sf,lower}} / \delta M_{\text{lower}}$.

The number density of galaxies that move into the higher mass bin due to star formation is then,

$$\delta \phi = \frac{\delta M_{\text{sf,lower}}}{\delta M_{\text{lower}}} \phi_{\text{lower}} = \frac{\psi_{\text{sf,lower}} \cdot \tau(z_2 - z_1)}{\delta M_{\text{lower}}} \quad (10)$$

Since we assume that the original galaxies are distributed evenly throughout a bin, then the fraction of galaxies in the lower mass bin which move into the higher mass bin is similar to the fraction of mass that moves up. In this case, the average mass of the galaxies brought up into the higher mass bin will be $0.5(M_{\text{top}} - \delta M_{\text{sf,lower}})$. Where M_{top} is the upper mass limit of the lower mass bin from which these galaxies are taken from. The amount of mass added to the higher mass bin due to star formation bringing up galaxies is therefore,

$$\Sigma M_{\text{sf}}^{\uparrow} = 0.5(M_{\text{top}} - \delta M_{\text{sf,lower}}) \cdot \delta \phi + \Sigma M_{\text{sf,lower}} \frac{\delta M_{\text{sf,lower}}}{\delta M_{\text{lower}}}, \quad (11)$$

where $\Sigma M_{\text{sf,lower}}$ is the total amount of star formation occurring in galaxies in the lower mass bin. In this case, $\Sigma M_{\text{sf,lower}} = \psi_{\text{sf,lower}} \cdot \tau(z_2 - z_1)$ (cf. eq. 8).

To determine how star formation in lower mass bins can affect the mass and number densities in higher mass bins we take the example of galaxies in the $10^{11} - 10^{11.5} M_{\odot}$ bin moving into the $M_* > 10^{11.5} M_{\odot}$ bin between $z \sim 1.3$ and $z \sim 1.1$.

In this case $\Sigma M_{\text{sf,lower}} = \psi_{\text{sf,lower}} \cdot \tau(z_2 - z_1) = 4.7 \times 10^6 h_{70}^3 M_{\odot} \text{Mpc}^{-3}$, and $\delta M_{\text{sf,lower}} = \psi_{\text{sf,lower}} \cdot \tau(z_2 - z_1) / \phi_{\text{lower}} = 4.3 \times 10^{10} M_{\odot}$. Since $\delta M_{\text{lower}} = 10^{11.5} M_{\odot} - 10^{11} M_{\odot} = 2.2 \times 10^{11} M_{\odot}$, then the fraction of galaxies in the lower mass bin at $z \sim 1.3$ which are now in the upper mass bin at $z \sim 1.1$ is $0.195 \times \phi_{\text{lower}}$. The change in number density in the upper mass bin, in our example, $M_* > 10^{11.5} M_{\odot}$, is then $4.3 \times 10^{-5} \text{Mpc}^{-3} \text{dex}^{-1}$. This is nearly entirely the difference between the number densities for galaxies at $z \sim 1.3$ and $z \sim 1.1$ for galaxies with masses $M_* > 10^{11.5} M_{\odot}$.

5.2 Mass Density Evolution and Merging

We calculate in the previous section that in the highest redshift bin there is no need for additional galaxies due to merging using the observed change in number densities. However, a better test of the merger scenario is to examine how the total mass densities evolve. The reason is that when mergers occur within a given mass bin the number density will decrease, but the mass density remains conserved, if no star formation is triggered. Because star formation and perhaps merging is occurring within lower mass galaxies, those systems will enter the higher mass bin and increase the number of galaxies, creating a static number number density, masking real evolution. However, in this case the integrated mass density must increase within our observed bin.

We continue our examination of mass transfer between the $M_* > 10^{11.5} M_{\odot}$ and $10^{11} M_{\odot} < M_* < 10^{11.5} M_{\odot}$ mass bins. We calculate the amount of mass added to the $M_* > 10^{11.5} M_{\odot}$ bin by subtracting the amount of mass added from star formation from the total mass density change. The amount of stellar mass added to the $M_* > 10^{11.5} M_{\odot}$ bin from star formation in the $10^{11} M_{\odot} < M_* < 10^{11.5} M_{\odot}$ bin is given by eq. (11). In this case, $\Sigma M_{\text{sf}}^{\uparrow} = 3.9 \times 10^6 h_{70}^3 M_{\odot} \text{Mpc}^{-3}$. The total integrated stellar mass added to galaxies at $M_* > 10^{11.5} M_{\odot}$ due to galaxies at $10^{11} M_{\odot} < M_* < 10^{11.5} M_{\odot}$ moving into the $M_* > 10^{11.5} M_{\odot}$ limit from star formation is shown in Figure 14 as the long-dashed red line.

This additional mass accounts for roughly half of the mass increase in the $M_* > 10^{11.5} M_\odot$ bin up to $z \sim 0.8$, with the remainder of the mass possibly originating from merging in the upper part of the $10^{11} M_\odot < M_* < 10^{11.5} M_\odot$ bin. We however cannot rule out that the scenario that mergers are not needed to account for the change in mass densities as the star formation from the lower mass bin is only lower than the change in mass densities by 1σ . By subtracting the star formation within the $M_* > 10^{11.5} M_\odot$ bin, and the mass added from star formation in the lower mass bin, we calculate $\Sigma M_{\text{merg}}^\dagger = 3.3 \times 10^6 h_{70}^3 M_\odot \text{Mpc}^{-3}$ using eq. (7).

To calculate the number of possible mergers, and the merger fraction within the $10^{11} M_\odot < M_* < 10^{11.5} M_\odot$ bin, we first must recognise which types of mergers, and of what masses, can enter the $M_* > 10^{11.5} M_\odot$ bin. First, to simplify things, we assume that galaxies within a given mass range and redshift range undergo at maximum one merger between z_1 and z_2 . This is a very reasonable assumption within our redshift bins given that even the fastest mergers take around 0.5 Gyr to complete. We furthermore assume that all mergers within the lower mass bin are major mergers of equal mass. With these assumptions, it is clear that only galaxies with $M_* > M_{\text{top}}/2$ will have a mass $M_* > M_{\text{top}}$ after merging with a galaxy of similar mass. Therefore, only galaxies merging with masses between $M_* = M_{\text{top}}/2$, and $M_* = M_{\text{top}}$ will enter the upper mass bin. If we assume that galaxies are evenly distributed between these two masses, then the average mass of a merging galaxy is $0.5(M_{\text{top}}/2 + M_{\text{top}})$, or $3/4M_{\text{top}}$. The total number density of galaxies merging¹, (n_{mg}), is therefore equal to the stellar mass density of galaxies which have merged divided by the average mass of the merging galaxies,

$$n_{\text{mg}} = \frac{4\Sigma M_{\text{merg}}^\dagger}{3M_{\text{top}}}. \quad (12)$$

We can compute the galaxy merger fraction (Conselice 2006), f_{mg} , as the total number of galaxies undergoing a merger divided by the total number of galaxies within a given bin. This fraction can then be expressed as,

$$f_{\text{mg}} \approx \frac{4\Sigma M_{\text{merg}}^\dagger}{3(\phi_{\text{lower}})(M_{\text{top}})}. \quad (13)$$

Plugging in numbers for our $10^{11} M_\odot < M_* < 10^{11.5} M_\odot$ and $M_* > 10^{11.5} M_\odot$ mass bins, we find that 12% of the galaxies with $10^{11} M_\odot < M_* < 10^{11.5} M_\odot$ merge between $z \sim 1.2 - 1.4$, and thus enter the higher mass bin. We find that at $z \sim 0.8 - 1.0$ this merger fraction drops to 8%. This is consistent with the CAS results presented in §4.3.5, and previous published results (Conselice et al. 2003; Lin et al. 2004; Bundy et al. 2004; Lotz et al. 2006; Bridge et al. 2007). This suggests that although number and mass densities do not statistically differ from each other, by examining the mass function in narrow redshift bins as well as the star formation rate and morphologies we conclude that there is additional mass added to these systems, by as much as a factor of two increase since $z \sim 1.4$, which is largely due to merging. Previously, we could not rule out no change in number densities,

¹ Note that the total number of galaxies merging is not the same as the total number of galaxy mergers, which is a factor of two lower.

based only on counting galaxies. The evolution is however clearly seen in the structures of these galaxies.

5.3 Comparison to models

We also compare our stellar mass and number densities results to models from e.g., De Lucia et al. (2006) based on the Millennium Simulation (Lemson et al. 2006) as another approach towards understanding how well we can reproduce with simulations the evolution of these systems. The Millennium Run is a Λ CDM simulation of the universe using 10^{10} particles and follows the dark matter and stellar assembly of galaxies in a $500h^{-1} \text{Mpc}$ cube. It is currently one of the most advanced simulations that are available for comparison to data, and have been used previously to trace the evolution of massive galaxies (De Lucia et al. 2006).

While the λ CDM model is very successful in explaining the large scale structure of the universe, there are inconsistencies when comparisons are done on the scale of galaxies. By testing this model in other ways, such as through the assembly of the most massive galaxies, we can perhaps determine the origin of some of the missing physics, or initial conditions used in these simulations.

The stellar mass calculation in the Millennium simulation uses the same IMF as our stellar mass measurements, and are based purely on the amount of stars produced in galaxies as a function of time. The Chabrier IMF enters into these models through the computation of the fraction of gas in star formation which is returned to the cold gas, which in these models is 40%. There is also a prescription for which stars explode as supernova, and when, which further reduces the stellar mass, but only for the stars at the highest masses.

When we compare our stellar mass number and mass densities to the Millennium model, we find that they generally underestimate the number and mass densities of the most massive galaxies at $z < 2$ (Figure 16). The agreement for both stellar mass number and mass densities at $z \sim 0$ is however fairly good within the uncertainties. The best agreement is between the number densities of systems with $10^{11} M_\odot < M_* < 10^{11.5} M_\odot$. However, as can be seen in Figure 16, this agreement breaks down when comparing the mass densities of these systems to the model. As there is generally a much worse agreement for the $M_* > 10^{11.5} M_\odot$ systems in terms of mass densities than number densities, we can interpret these disagreements in the sense that the models do not produce enough massive galaxies early enough. This extends throughout the $M_* > 10^{11} M_\odot$ range. Clearly, the models eventually produce these massive systems, as there is agreement at $z \sim 0$, but they are formed in the simulation at much later times, typically at $z < 1$ through mergers (De Lucia et al. 2006).

This disagreement suggests that the bulk formation of massive galaxy formation occurs at $z > 2$, especially for the massive systems. This implies both an early star formation history, as well as an early mass assembly history. When comparing with observations of the merger history, it is clear that massive galaxies are formed through mergers at $z > 2$ (Conselice 2006). It is likely that these galaxies are much more biased than what the Millennium simulation assumes, and thus they must have an early merger and star formation history.

When examining the galaxy merger history (Conselice et al. 2003; Conselice 2006), it is clear that massive galaxies do not merge much at $z < 2$, but have a high merger fraction ($\sim 50\%$) at higher redshifts, $z > 2$. The Millennium model produces most of the mass in these massive galaxies by $z \sim 2$, but they are not yet assembled in massive galaxies in the model until relatively late (e.g., De Lucia et al. 2006). It appears that the actual merger rate for massive galaxies is much higher in the past, than what is predicted, and likewise smaller at $z < 2$ than the models.

6 SUMMARY

We utilise wide and deep near infrared imaging from the Palomar telescope combined with DEEP2 spectroscopy to select and study the properties and evolution of $M_* > 10^{11} M_\odot$ galaxies found at $0.4 < z < 1.4$. Our total sample consists of 4571 galaxies with $M_* > 10^{11} M_\odot$, and 225 galaxies with $M_* > 10^{11.5} M_\odot$. We investigate with DEEP2 spectroscopy, Hubble Space Telescope (HST) imaging, Chandra imaging, and Spitzer MIPS imaging; the X-ray, morphological and star forming properties of our sample. Our major findings are:

1. The stellar mass and number densities of $M_* > 10^{11} M_\odot$ galaxies does not change significantly at $z < 1$. We however cannot rule out factors of 2-3 in number and mass density evolution for these systems, based solely on densities, due to uncertainties in these measurements. Systems with $10^{11} M_\odot < M_* < 10^{11.5} M_\odot$ however show a significant increase between $z \sim 1 - 1.5$. The increase in stellar mass density for systems with $M_* > 10^{11.5} M_\odot$ is however marginally insignificant over our entire redshift range up to $z \sim 2$.

2. There is a diversity in the morphological properties of galaxies selected solely by stellar mass. We find that most galaxies selected with $M_* > 10^{11.5} M_\odot$ are classifiable as early-types at all redshifts, with only a small fraction classified as peculiars and spirals at $z \sim 1.3$. Systems with $10^{11} M_\odot < M_* < 10^{11.5} M_\odot$ have a lower fraction of galaxies consistent with being early-types, with a nearly constant fraction with redshift of 70%. The remaining systems tend to be classified as peculiars/mergers at high redshift, and spirals at lower redshifts. We further find that a significant number of the early-type galaxies contain a slight morphological disturbance, which is furthermore seen in the quantitative CAS parameters.

3. We find that a significant fraction ($\sim 40\%$) of massive galaxies at $0.4 < z < 1.4$ are undergoing star formation. This is demonstrated through the blue colours of massive galaxies, and star formation rates as derived through Spitzer MIPS imaging of these systems. The fraction of galaxies with $M_* > 10^{11.5} M_\odot$ which are on the red-sequence is only 60% at $z \sim 1.3$, but increases to $\sim 100\%$ by $z \sim 0.4$. Likewise, the fraction of lower mass systems, with $10^{11} M_\odot < M_* < 10^{11.5} M_\odot$, which are on the red-sequence increases with time, although at every redshift there is a higher fraction of systems with $M_* > 10^{11.5}$ on the

red-sequence than at lower masses.

4. We investigate the star formation rate density for our massive galaxy sample, finding a steep decline in the star formation rate density for systems with $M_* > 10^{11.5} M_\odot$, and a more shallower decline for systems with $10^{11} M_\odot < M_* < 10^{11.5} M_\odot$. The rate of decline in star formation for $M_* > 10^{11.5} M_\odot$ systems can be parameterised as $(1+z)^{6\pm 2.2}$, as opposed to $(1+z)^{4\pm 0.6}$ for systems with masses $10^{11} M_\odot < M_* < 10^{11.5} M_\odot$.

5. We match our catalog of massive galaxies to a catalog of X-ray sources discovered with Chandra imaging in our largest field, the Extended Groth Strip. We find that a significant fraction (5%) of the most massive galaxies are X-ray emitting AGN. We investigate in detail the properties of these AGN and find that the most massive galaxies, with $M_* > 10^{11.5} M_\odot$, have soft hardness ratios, while the galaxies with $10^{11} M_\odot < M_* < 10^{11.5} M_\odot$ have a mixture of hard and soft ratios. Furthermore, we find that nearly half of all the massive galaxies which have AGN are either distorted ellipticals or peculiars.

6. We investigate how much stellar mass is added to galaxies due to star formation from $z \sim 1.4$ to $z \sim 0.4$, and compare this to the observed changes in the stellar mass density. We find to $> 3\sigma$ confidence that the star formation seen in individual massive galaxy bins at $z < 1.4$ cannot account for the changes in stellar mass seen in galaxies with $M_* > 10^{11} M_\odot$. We however find that the amount of mass which transfers between bins due to star formation, bringing galaxies up into higher mass bins, can within 1σ account for this increase. The difference suggests that up to a single major merger is occurring for $M_* > 10^{11} M_\odot$ galaxies at $0.4 < z < 1.4$. This is also found to be the case through an analysis of CAS parameters, giving $0.9_{-0.5}^{+0.7}$ major mergers at $0.4 < z < 1.4$.

Our major conclusion in this paper is that the stellar mass assembly of massive galaxies is, within a factor of two, complete by $z \sim 1$. There is however still significant morphological and colour evolution at $z < 1$ for massive galaxies. We also find significant evolution in the number and mass densities for galaxies with $M_* > 10^{11} M_\odot$ at $z > 1$. Furthermore, we have shown that the study of ‘early-types’, defined through colour, morphology or mass, at high redshifts must be carefully done, and results of studies will vary significantly, depending on selection. It is clear, particularly at high redshift, that red galaxies are not the equivalent of massive galaxies, or elliptical galaxies, and each of these populations must be studied individually.

The Palomar and DEEP2 surveys would not have been completed without the active help of the staff at the Palomar and Keck observatories. We thank Niv Drory, Karl Glazebrook, Gabriella De Lucia, Gerard Lemson & the Virgo Consortium for providing data in an electronic formation, and Sandy Faber and the anonymous referee for their comments on this work. We thank Stephen Bevan for computing stellar masses using both the Bruzual & Charlot (2003) and (2007) models, and we thank G. Bruzual and S Charlot for providing us with their 2007 models before publication. Funding to support this effort came from a National Science Foundation Astronomy & Astrophysics Fellowship, grants from the UK Particle Physics and Astronomy Research Coun-

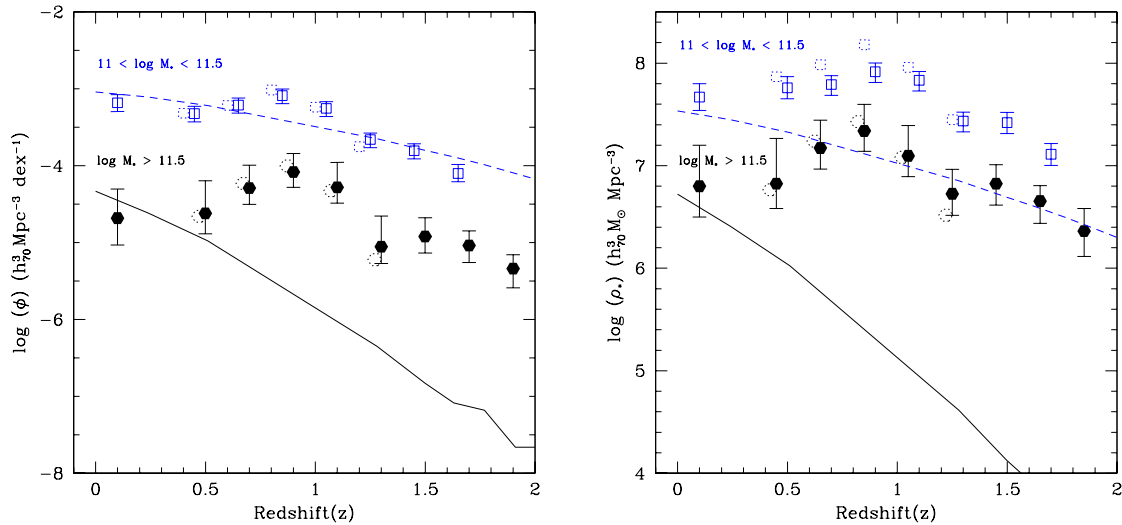


Figure 16. A comparison between our data and the models from the Millennium simulation (e.g., De Lucia et al. 2006). The data shown are the same for the massive galaxy sample plotted in Figure 4. The dashed line shows the predicted evolution in the number and stellar mass densities for $10^{11} M_{\odot} < M_{*} < 10^{11.5} M_{\odot}$ systems, while the solid line shows the same predicts for galaxies with stellar masses $M_{*} > 10^{11.5} M_{\odot}$. As can be seen, for the most part the simulated massive galaxies do not assembly quickly enough to match the observations.

cil (PPARC), Support for the ACS imaging of the EGS in GO program 10134 was provided by NASA through NASA grant HST-G0-10134.13-A from the Space Telescope Science Institute, which is operated by the Association of Universities for Research in Astronomy, Inc., under NASA contract NAS 5-26555. This work is based, in part, on observations made with the Spitzer Space Telescope, which is operated by the Jet Propulsion Laboratory, California Institute of Technology under a contract with NASA. Support for this work was provided by NASA through contract 1255094 issued by JPL/Caltech.

The authors wish to recognise and acknowledge the very significant cultural role and reverence that the summit of Mauna Kea has always had within the indigenous Hawaiian community. We are most fortunate to have the opportunity to conduct observations from this mountain. ALC/JAN is supported by NASA through Hubble Fellowship grant HF-01182.01-A/HF-011065.01-A. Support for this work was also provided by NASA to CJP through the Spitzer Space Telescope Fellowship Program, through a contract issued by the Jet Propulsion Laboratory, California Institute of Technology under a contract with NASA.

REFERENCES

- Abadi, M.G., Navarro, J.F., Steinmetz, M., Eke, V.R. 2003, *ApJ*, 591, 499
- Baldry, I.K., Glazebrook, K., Brinkmann, J., Ivezić, Z., Lupton, R.H., Nichol, R.C., Szalay, A.S. 2004, *ApJ*, 600, 681
- Bell, E.F., et al. 2004, *ApJ*, 608, 752
- Bell, E., et al. 2005, *ApJ*, 625, 23
- Bell, E., et al. 2006, *ApJ*, 640, 241
- Benitez, N. 2000, *ApJ*, 536, 571
- Bershady, M.A., Jangren, J.A., Conselice, C.J. 2000, *AJ*, 119, 2645
- Bertin, E., & Arnouts, S. 1996, *A&AS*, 117, 393
- Borch, A., et al. 2006, *A&A*, 453, 869
- Bouche, N., et al. 2007, eprint arXiv:0706.2656
- Bridge, C., et al. 2007, *ApJ*, 659, 931
- Brinchmann, J., Ellis, R.S. 2000, *ApJ*, 536, 77L
- Brown, M.J.I., Dey, A., Jannuzi, B.T., Brand, K., Benson, A.J., Brodwin, M., Croton, D.J., Eisenhardt, P.R. 2007, *ApJ*, 654, 858
- Bruzual, G., Charlot, S. 2003, *MNRAS*, 344, 1000
- Bruzual, G. astro-ph/0703052
- Bundy, K., Fukugita, M., Ellis, R., Kodama, T., Conselice, C.J. 2004, *ApJ*, 601, 123L
- Bundy, K., et al. 2006, *ApJ*, 651, 120
- Bundy, K., Ellis, R.S., Conselice, C.J. 2005, *ApJ*, 625, 621
- Cassata, P., et al. 2005, *MNRAS*, 357, 903
- Chabrier, G. 2003, *ApJ*, 586, 133L
- Cimatti, A., Daddi, E., Renzini, A. 2006, *A&A*, 453, L29
- Coil, A.L., et al. 2004a, *ApJ*, 609, 525
- Coil, A.L., et al. 2004b, *ApJ*, 617, 765
- Collister, A.A., Lahav, O. 2004, *PASP*, 116, 345
- Cole, S., et al. 2001, *MNRAS*, 326, 255
- Conselice, C.J. 1997, *PASP*, 109, 1251
- Conselice, C.J., Bershady, M.A., Jangren, A. 2000a, *ApJ*, 529, 886
- Conselice, C.J., Bershady, M.A., Gallagher, J.S. 2000b, *A&A*, 354, 21L
- Conselice, C.J., Gallagher, J.S., Calzetti, D., Homeier, N., Kinney, A. 2000c, *AJ*, 119, 79
- Conselice, C.J. 2003, *ApJS*, 147, 1
- Conselice, C.J., Bershady, M.A., Dickinson, M., Papovich, C. 2003a, *AJ*, 126, 1183
- Conselice, C.J., Chapman, S.C., Windhorst, R.A. 2003b,

ApJ, 596, 5L
 Conselice, C.J., Gallagher, J.S., Wyse, R.F.G. 2002, AJ, 123, 2246
 Conselice, C.J., et al. 2004, ApJ, 600, 139L
 Conselice, C.J., Blackburne, J., Papovich, C. 2005a, ApJ, 620, 564
 Conselice, C.J., Bundy, K., Ellis, R., Brichmann, J., Vogt, N., Phillips, A. 2005b, ApJ, 628, 160
 Conselice, C.J. 2006a, MNRAS, 373, 1389
 Conselice, C.J. 2006b, ApJ, 638, 686
 Conselice, C.J., et al. 2007, ApJ, 660, 55L
 Daddi, E., et al. 2004, ApJ, 600, 127L
 Dale, D.A., Helou, G. 2002, ApJ, 576, 159
 Davis, M., et al. 2003, SPIE, 4834, 161
 Davis, M., et al. 2007, ApJ, 660, 1L
 De Lucia, G., Springel, V., White, S.D.M., Croton, D., Kauffmann, G. 2006, MNRAS, 366, 499
 Dickinson, M., Papovich, C., Ferguson, H.C., Budavári, T. 2003, ApJ, 587, 25
 Donas, J., et al. 2006, astro-ph/0608594
 Drory, N., Bender, R., Feulner, G., Hopp, U., Maraston, C., Snigula, J., Hill, G.J. 2004, ApJ, 608, 742
 Drory, N., Salvato, M., Gabasch, A., Bender, R., Hopp, U., Feulner, G., & Pannella, M. 2005, ApJ, 619, L131
 Dunlop, J., Peacock, J., Spinrad, H., Dey, A., Jimenez, R., Stern, D., Windhorst, R. 1996, Nature, 381, 581
 Elmegreen, D.M., Elmegreen, B.G., Rubin, D.S., Schaffer, M.A. 2005, ApJ, 631, 85
 Elston, R., Rieke, G.H., Rieke, M.J. 1988, ApJ, 331, 77L
 Erb, D.K., et al. 2003, ApJ, 591, 101
 Faber, S., et al. 2003, SPIE, 4841, 1657
 Faber, S., et al. 2005, astro-ph/0506044
 Fontana, A., et al. 2004, A&A, 424, 23
 Forster-Schreiber, N.M., et al. 2006, ApJ, 645, 1062
 Foucaud, S., et al. 2007, MNRAS, 376, 20L
 Genzel, R., et al. 2006, Nature, 442, 786
 Georgakakis, A., et al. 2006, astro-ph/0606139
 Giavalisco, M., et al. 2004, ApJ, 600, 93L
 Glazebrook, K., et al. 2004, Nature, 430, 181
 Graham, A.W., Driver, S.P., Petrosian, V., Conselice, C.J., Bershad, M.A., Crawford, S.M., Goto, T. 2005, AJ, 130, 1535
 Graham, J.R., Dey, A. 1996, ApJ, 471, 720
 Grazian, A., et al. 2006, A&A, 465, 393
 Grogin, N.A., et al. 2005, ApJ, 627, 97L
 Hernandez-Toledo, H.M., Avila-Reese, V., Conselice, C.J., Puerari, I. AJ, 2005, AJ, 129, 682
 Hernandez-Toledo, H.M., Avila-Reese, V., Salazar-Contreras, J.R., Conselice, C.J. 2006, AJ, 132, 71
 Hopkins, A. 2004, ApJ, 615, 209
 Hornschemeier, A.E., et al. 2003, AJ, 126, 575
 Im, M., et al. 2002, ApJ, 571, 136
 Jogee, S., et al. 2004, ApJ, 615, 105L
 Juneau, S., et al. 2005, ApJ, 619, 135
 Kannappan, S.J., & Gawiser, E. 2007, ApJ, 657, 5L
 Kriek, M., et al. 2006, ApJ, 649, L71
 Labbe, I., et al. 2003, ApJ, 591, 95L
 Labbe, I., et al. 2005, ApJ, 624, 81L
 Lane, K.P., et al. 2007, MNRAS, ??, 55L, arXiv:0704.2136
 Larson, R.B. 1974, MNRAS, 166, 585L
 Le Fevre, O., et al. 2000, MNRAS, 311, 565
 Le Floch, E., et al. 2005, ApJ, 632, 169
 Lehmer, B.D., et al. 2005, AJ, 129, 1
 Lemson, G., et al. 2006, astro-ph/0608019
 Lilly, S., Le Fevre, O., Crampton, D., Hammer, F., Tresse, L. 1995, ApJ, 455, 50L
 Lin, L., et al. 2004, ApJ, 617, 9L
 Lotz, J.M., et al. 2006, astro-ph/0602088
 Maraston, C. 2005, MNRAS, 362, 799
 Menanteau, F., et al. 2005, ApJ, 620, 697
 Mobasher, B., Jogee, S., Dahlen, T., de Mello, D., Lucas, R.A., Conselice, C.J., Grogin, N.A., Livio, M. 2004, ApJ, 600, 143L
 Moustakas, L.A., et al. 2004, ApJ, 600, 131L
 Nandra, K., et al. 2006, astro-ph/0607270
 Noeske, K., et al. 2007a, ApJ, 660, 47L
 Noeske, K., et al. 2007b, ApJ, 660, 43L
 Papovich, C., Dickinson, M., Giavalisco, M., Conselice, C.J., Ferguson, H.C. 2005, ApJ, 631, 101
 Papovich, C., Giavalisco, M., Dickinson, M., Conselice, C.J., Ferguson, H.C. 2003, ApJ, 598, 827
 Papovich, C., et al. 2004, ApJS, 154, 70
 Papovich, C., et al. 2006, ApJ, 640, 92
 Patton, D.R., et al. 2002, ApJ, 565, 208
 Persson, S.E., Murphy, D.C., Krzeminski, W., Roth, M., Rieke, M.J. 1998, AJ, 116, 2475
 Ravindranath, S., et al. 2004, ApJ, 604, 9L
 Reddy, N.A., Steidel, C.C., Erb, D.K., Shapley, A.E., Pettini, M. 2006, ApJ, 653, 1004
 Rudnick, G., et al. 2006, ApJ, 650, 624
 Saracco, P., et al. 2005, MNRAS, 357, 40L
 Sawicki, M., Yee, H.K.C. 1998, 115, 1329
 Somerville, R.S., Lee, K., Ferguson, H.C., Gardner, J.P., Moustakas, L.A., Giavalisco, M. 2004, 600, 171L
 Spinrad, H., Dey, A., Stern, D., Dunlop, J., Peacock, J., Jimenez, R., Windhorst, R. 1997, ApJ, 484, 581
 Stanford, S.A., Dickinson, M.E., Postman, M., Ferguson, H.C., Lucas, R.A., Conselice, C.J., Budavari, T., Somerville, R. 2004, AJ, 127, 131
 Steidel, C.C., Shapley, A.E., Pettini, M., Adelberger, K.L., Erb, D.K., Reddy, N.A., Hunt, M.P. 2004, ApJ, 604, 534
 Strateva, I., et al. 2001, AJ, 122, 1861
 Taylor-Mager, V., Conselice, C., Windhorst, R., Jansen, R. 2007, ApJ, 659, 162
 Teplitz, H.I., et al. 2006, AJ, 132, 853
 Treu, T., et al. 2005, ApJ, 633, 174
 Trujillo, I., et al. 2004, ApJ, 604, 521
 Trujillo, I., et al. 2006, MNRAS, 373, 36L
 Weiner, B.J., et al. 2006, ApJ, 660, 39L
 White, S.D.M., Rees, M.J. 1978, MNRAS, 183, 341
 Willmer, C.N.A., et al. 2006, ApJ, 647, 853
 Windhorst, R., et al. 2002, ApJS, 143, 113
 Worthey, G. 1994, ApJS, 95, 107
 Yan, R., Newman, J.A., Faber, S.M., Konidaris, N., Koo, D., Davis, M. 2006, ApJ, 648, 281

APPENDIX A: CAS VS. VISUAL MORPHOLOGIES

In this appendix we describe in more detail the degree of agreement between the CAS and visual estimates of morphology. We are particularly interested in describing why some systems classified as a particular type by eye fall into

a different region of CAS space than what their apparent morphology would indicate. A more limited discussion of this issue has been presented in Conselice (1997), Bershady et al. (2000), Mobasher et al. (2004) and Conselice et al. (2005a).

Before we discuss why there are differences between visual estimates of morphological type and the quantitative approach, it is important to describe the process of morphological classification by eye. This process was carried out by one of us (CJC) by examining a galaxy's structure on a computer screen. This was done through IRAF and the viewing tool DS9, although similar results can be had through any approach that lets the viewer change the contrast. Classification was done into the types described in §4.3 using the traditional approach of examining the entire galaxy at once, and judging which of the categories it belongs to. When this process is done we do not take into account the smaller, more subtle, details of a galaxy's structure. For example, although most of our sample of $> 10^{11} M_{\odot}$ galaxies consists of ellipticals, about a third have some kind of morphological peculiarity. Typically, this was either a diffuse outer envelope of material, or a lopsided centre with respect to the rest of the galaxy. This is clearly seen the CAS space for these systems - the peculiar ellipticals have higher asymmetry and clumpiness values than ellipticals, compacts and S0s.

However, there are cases in which a galaxy has been classified as one type but appears in a region of the CAS space where it ordinarily should not be. Examples of this include ellipticals with high asymmetries, or low concentrations, and peculiar galaxies with low asymmetries. While on average these galaxy populations are found in the location expected within the CAS space, there are some obvious exceptions. After creating the first version of Figure 9 we went back and examined by eye the $\sim 5\%$ of galaxies whose visual morphology differed greatly from their measured CAS values. About half of the time it turned out that the galaxy was misclassified by eye or recorded incorrectly. This always accounted for the most obvious cases where the CAS values and eye estimates of morphology differed the most.

There are however systems that still differ in terms of their visual estimates of morphology and their measured CAS values. It turns out that the CAS parameters are most successful at distinguishing disk galaxies, ellipticals and mergers from each other (Cassatta et al. 2005). We therefore focus on these three populations. First, perhaps the most obvious disagreement is the high-A ellipticals and the low-A peculiars. The ellipticals classified by eye that contain a high asymmetry were nearly always systems that had some morphological peculiarity. In other cases, it was determined that the high-A elliptical/S0 systems were nearly edge-on, or otherwise peculiar, S0s that often contained a prominent dust lane. Other examples were ellipticals that contained neighbouring galaxies that created a higher-A signal.

The peculiars that are at $A < 0.3$ show a diversity of visual morphologies. Often these systems were compact and concentrated with some diffuse material, or had blob like features nearby. In many cases these systems appear to be ellipticals in assembly, and could have easily been classified as peculiar ellipticals. Other examples of lower-A peculiars are systems imaged with a low-S/N. As has been argued in Conselice et al. (2000) and Conselice (2003) a lower S/N will make it more difficult to measure quantitative indices

for these systems. Several systems resembled spiral galaxies, or spirals in assembly, with what appears to be arms in development. It thus appears that quantitative measures of structures are revealing information that eye-ball estimates are missing, namely that a gross morphology can be present while the galaxy structure still retains some signatures of recent formation. This creates significant differences when comparing galaxies of the same type, as selected by eye-ball estimates, at low and high redshifts.